

# Octupole correlations in collective excitations of neutron-rich $N \approx 56$ nuclei

Kosuke Nomura\*

*Department of Physics, Faculty of Science, University of Zagreb, HR-10000 Zagreb, Croatia*

(Dated: April 6, 2022)

Octupole correlations in the low-energy collective states of neutron-rich nuclei near the neutron number  $N = 56$  are studied within the interacting boson model (IBM) based on the nuclear density functional theory. The constrained self-consistent mean-field (SCMF) calculations using a universal energy density functional and a pairing interaction provide the potential energy surfaces in terms of the axially-symmetric quadrupole and octupole deformations for the even-even nuclei  $^{86-94}\text{Se}$ ,  $^{88-96}\text{Kr}$ ,  $^{90-98}\text{Sr}$ ,  $^{92-100}\text{Zr}$ , and  $^{94-102}\text{Mo}$ . Spectroscopic properties are computed in terms of the IBM that consists of the monopole  $s$ , quadrupole  $d$ , and octupole  $f$  bosons. Strength parameters for the boson Hamiltonian are determined by mapping the SCMF energy surface onto the expectation value of the Hamiltonian in the boson condensate state. At the SCMF level, no octupole deformed ground-state shape is found, while the energy surface is generally soft in the octupole deformation at  $N \approx 56$ . The predicted negative-parity yrast bands with the bandhead state  $3_1^-$  weakly depend on  $N$  and become lowest in energy at  $N = 56$  in each of the considered isotopic chains. The model further predicts finite electric octupole transition rates between the lowest negative-parity and the positive-parity ground-state bands.

## I. INTRODUCTION

The ground-state shape and the related spectroscopic properties of those neutron-rich nuclei in the mass  $A \approx 100$  region have been of considerable interest. The low-energy structure of these nuclei depends on the underlying shell structures and nuclear forces, and is characterized by a subtle interplay between the single-particle and collective degrees of freedom. A number of nuclei belonging to this mass region have been suggested to demonstrate intriguing nuclear shape-related features that include the triaxial deformation, the proton  $Z = 40$  and neutron  $N = 56$  sub-shell gaps, the coexistence of several different shapes in the vicinity of the ground state [1], the quantum phase transitions in their shapes [2] represented by a sudden onset of deformation near the neutron number  $N \approx 60$ .

Of particular interest is the octupole correlations and the related low-energy negative-parity states. In a simple spherical shell model, the octupole correlations become enhanced in particular mass regions in the nuclear mass table, in which the coupling between the normal and unique parity single-particle orbitals in a given major oscillator shell that satisfy the conditions  $\Delta\ell = \Delta j = 3\hbar$  is possible, with  $\ell$  and  $j$  the quantum numbers for a single-particle state. The so-called “octupole magic numbers” at which the above conditions are met and stable octupole deformations are supposed to emerge are the neutron and/or proton numbers 34, 56, 88, 134, ... [3, 4]. Experimental evidence for the permanent octupole deformations were found at CERN in the light actinides with  $(N, Z) \approx (134, 88)$  such as  $^{220}\text{Rn}$  and  $^{224}\text{Ra}$  [5], and  $^{228}\text{Th}$  [6] and at ANL in the lanthanides with  $(N, Z) \approx (88, 56)$  such as  $^{144}\text{Ba}$  [7] and  $^{146}\text{Ba}$  [8]. On the other hand, the possible octupolarity in the lighter-mass

regions, such as those with  $(N, Z) \approx (56, 34)$ ,  $(56, 56)$  and  $(34, 34)$ , has not been as extensively investigated, both experimentally and theoretically, as in the cases of the actinides and lanthanides.

In some of the neutron-rich even-even Mo, Zr, Sr, and Kr isotopes that are in the vicinity of the neutron number  $N \approx 56$ , low-lying negative-parity state  $3^-$  at the excitation energy  $E_x \approx 2$  MeV as well as the band built on it have been suggested experimentally (see, e.g., Refs. [9–16]). The negative-parity states are supposed to appear as a consequence of the coupling between the neutron  $h_{11/2}$  and  $d_{5/2}$  orbitals. In the neutron-rich nuclei  $^{94,96}\text{Kr}$ , in particular, the  $3^-$  states have been newly obtained in an experiment at RIKEN [16]. With the recurrent interests in the studies of the octupole shapes and the new data on the negative-parity states in radioactive nuclei, it would be meaningful to pursue timely theoretical investigations to address the relevance of the octupole degrees of freedom in the description of low-lying nuclear structure in the neutron-rich  $A \approx 100$  region.

Theoretical approaches to the octupole deformations and collective excitations include the self-consistent mean-field (SCMF) framework based on the macroscopic-microscopic method with Strutinski shell correction [17–19] and the energy density functionals (EDFs) [20–37], the interacting boson model (IBM) [38–56], the geometrical collective model [57–60], the cluster models [61–63], and the nuclear shell model [64–67]. In particular, the SCMF methods using a given universal non-relativistic [34, 68] or relativistic [69, 70] EDF provides a global description of the bulk nuclear matter and intrinsic properties as well as collective excitations over the entire region of the nuclear mass table. In recent years, the EDF-based approaches have been extensively used for the studies of the octupole deformations and collectivity. A straightforward approach is the beyond SCMF calculations with symmetry projections and configuration mixing within the generator coordinate method (GCM)

\* knomura@phy.hr

[20–25, 27–29, 33, 34, 36, 71]. The full GCM calculations are, however, computationally so demanding that some alternative approaches have also been considered, such as the mapping onto the quadrupole-octupole collective Hamiltonian [26, 30, 37] and onto the interacting-boson Hamiltonian [48–50].

In this article, the octupole correlations and the relevant spectroscopic properties of the low-lying positive- and negative-parity states in the neutron-rich nuclei near the octupole magic number  $N = 56$  are investigated within the framework of the nuclear EDF and the mapped IBM. The starting point is the axially-symmetric quadrupole and octupole constrained SCMF calculations of the potential energy surfaces for those nuclei in which octupolarity is expected to be enhanced, i.e.,  $^{86-94}\text{Se}$ ,  $^{88-96}\text{Kr}$ ,  $^{90-98}\text{Sr}$ ,  $^{92-100}\text{Zr}$ , and  $^{94-102}\text{Mo}$ . Then, by using the method of Ref. [49] the quadrupole-octupole SCMF energy surface is mapped onto the equivalent one in the system of the interacting monopole  $s$ , quadrupole  $d$ , and octupole  $f$  bosons. The mapping procedure specifies the strength parameters for the  $sdf$ -IBM Hamiltonian, which in turn gives excitation spectra and electromagnetic transition rates of both the positive- and negative-parity states. Previously, the mapped  $sdf$ -IBM framework has been applied to the studies of octupole shape phase transitions in light actinides and rare-earth nuclei using the relativistic EDF [48, 49]. A number of spectroscopic calculations have been carried out based on the Gogny-type EDF [34], and revealed the onset of octupole deformations and collectivity in various mass regions characteristic of the octupole deformations [50–54].

In the present study, a version of the  $sdf$ -IBM that makes distinction between the neutron and proton boson degrees of freedom, denoted hereafter by  $sdf$ -IBM-2, is considered since it is more realistic than a simpler version of the IBM ( $sdf$ -, or  $spdf$ -IBM-1) that does not distinguish between the protons and neutrons. In most of the previous IBM calculations for the octupole collective states, the simple IBM-1 framework has been employed. There are a few instances in which the  $sdf$ -IBM-2 has been considered on phenomenological grounds, e.g., in Refs. [44, 46, 47, 56]. In this study, all the strength parameters for the  $sdf$ -IBM-2 are determined by using the microscopic input from the constrained SCMF calculations. As a basis of the SCMF method, the relativistic density-dependent point-coupling (DD-PC1) EDF [72] is employed. The universal functional DD-PC1 has been successfully employed in the spectroscopic studies on the octupole collective modes both at the static and beyond SCMF levels [31, 33, 37].

The paper is structured as follows. In Sec. II the theoretical procedure in the mapped  $sdf$ -IBM-2 calculations is illustrated. Results of the quadrupole-octupole constrained potential energy surfaces, the systematics of the low-energy spectra for the positive- and negative-parity states, electric quadrupole, octupole and dipole transition rates that characterize the octupole correlations in

the considered Se, Kr, Sr, Zr, and Mo nuclei are discussed in Sec. III. In the same section detailed level structures for the octupole magic nuclei, i.e., the  $N = 56$  isotones, are analyzed, with a special attention to the neutron-rich Kr isotopes where some updated experimental data are available. Finally, Sec. IV gives a summary of the main results and conclusions.

## II. THEORETICAL FRAMEWORK

The constrained SCMF calculations are performed within the relativistic Hartree-Bogoliubov (RHB) framework [69, 70, 73] using the DD-PC1 interaction for the particle-hole channel and a separable pairing force of finite range [74] for the particle-particle channel. Here the strength  $V_0 = 837 \text{ MeV fm}^3$  is used for both the proton and neutron pairs, and corresponds to an increase of the original value  $728 \text{ MeV fm}^3$  of Ref. [74]. The constraints imposed in the SCMF calculations are on the expectation values of the axially-symmetric quadrupole  $\hat{Q}_{20}$  and octupole  $\hat{Q}_{30}$  moments,

$$\hat{Q}_{20} = 2z^2 - x^2 - y^2, \quad (1)$$

$$\hat{Q}_{30} = 2z^3 - 3z(x^2 + y^2), \quad (2)$$

which are associated with the dimensionless quadrupole  $\beta_2$  and octupole  $\beta_3$  deformations through the relations

$$\beta_2 = \frac{\sqrt{5\pi}}{3r_0^2 A^{5/3}} \langle \hat{Q}_{20} \rangle \quad (3)$$

$$\beta_3 = \frac{\sqrt{7\pi}}{3r_0^3 A^2} \langle \hat{Q}_{30} \rangle \quad (4)$$

with  $r_0 = 1.2 \text{ fm}$ . The RHB equation is solved in a harmonic oscillator basis with the number of oscillator shells  $N_F = 12$ . The constrained calculations provide the potential energy surfaces  $E(\beta_2, \beta_3)$  as functions of the  $\beta_2$  and  $\beta_3$  deformations. The  $\beta_2 - \beta_3$  energy surface has a property that it is symmetric with respect to the  $\beta_3 = 0$  axis, i.e.,  $E(\beta_2, \beta_3) = E(\beta_2, -\beta_3)$ , and it is therefore enough to consider the part of the energy surface with  $\beta_3 \geq 0$ .

The  $sdf$ -IBM-2 is comprised of the neutron and proton monopole  $s_\nu$  and  $s_\pi$ , quadrupole  $d_\nu$  and  $d_\pi$ , and octupole  $f_\nu$  and  $f_\pi$  bosons, which are, from a microscopic point of view [75, 76], associated with the correlated pairs of valence neutrons and protons with spin and parity  $J = 0^+$ ,  $2^+$ , and  $3^-$ , respectively. The calculations are carried out within the neutron  $N = 50 - 82$  and proton  $Z = 28 - 50$  major shells and, therefore, the doubly-magic nucleus  $^{78}\text{Ni}$  is taken as the inert core. The number of the neutron (or proton) bosons  $n_\nu$  (or  $n_\pi$ ) is conserved for each nucleus, and is equal to half the number of valence neutron (or proton) pairs. The neutron (or proton)  $s_\nu$  ( $s_\pi$ ),  $d_\nu$  ( $d_\pi$ ), and  $f_\nu$  ( $f_\pi$ ) bosons, denoted by  $n_{s_\nu}$ ,  $n_{d_\nu}$ , and  $n_{f_\nu}$  ( $n_{s_\pi}$ ,  $n_{d_\pi}$ , and  $n_{f_\pi}$ ), respectively, satisfy the condition that  $n_{s_\nu} + n_{d_\nu} + n_{f_\nu} = n_\nu$  (or  $n_{s_\pi} + n_{d_\pi} + n_{f_\pi} = n_\pi$ ).

Based on the earlier microscopic considerations [75] that the low-lying structure of medium-heavy and heavy nuclei is mainly determined by the pairing-like correlations between identical nucleons and the quadrupole-quadrupole interactions between non-identical nucleons, the following form of the *sdf*-IBM-2 Hamiltonian is adopted:

$$\hat{H} = \epsilon_d \hat{n}_d + \epsilon_f \hat{n}_f + \kappa_2 \hat{Q}_\nu \cdot \hat{Q}_\pi + \kappa_3 \hat{O}_\nu \cdot \hat{O}_\pi. \quad (5)$$

The first (second) term stands for the  $d$  ( $f$ ) boson number operator  $\hat{n}_d = \hat{n}_{d_\nu} + \hat{n}_{d_\pi}$  ( $\hat{n}_f = \hat{n}_{f_\nu} + \hat{n}_{f_\pi}$ ) with the single  $d$  ( $f$ ) boson energy  $\epsilon_d$  ( $\epsilon_f$ ) relative to the  $s$  boson one. The single boson energies,  $\epsilon_d$  and  $\epsilon_f$ , could in principle be different, but are here assumed to be the same for simplicity, between the neutron and proton bosons. The third term is the quadrupole-quadrupole interaction with the strength  $\kappa_2$ , and the quadrupole operator is given by

$$\hat{Q}_\rho = s_\rho^\dagger \tilde{d}_\rho + d_\rho^\dagger s_\rho + \chi_\rho (d_\rho^\dagger \times \tilde{d}_\rho)^{(2)} + \chi'_\rho (f_\rho^\dagger \times \tilde{f}_\rho)^{(2)} \quad (6)$$

for neutron  $\rho = \nu$  and proton  $\rho = \pi$ .  $\chi_\rho$  and  $\chi'_\rho$  are dimensionless parameters. The last term in (5) represents the octupole-octupole interaction between the neutron and proton bosons with the strength  $\kappa_3$  and the octupole

operator is given as

$$\hat{O}_\rho = s_\rho^\dagger \tilde{f}_\rho + f_\rho^\dagger s_\rho + \chi''_\rho (d_\rho^\dagger \times \tilde{f}_\rho + f_\rho^\dagger \times \tilde{d}_\rho)^{(3)}, \quad (7)$$

with another dimensionless parameter  $\chi''_\rho$ .

To make a connection between the geometrical structure of a multifermion systems specified by the  $\beta_2$  and  $\beta_3$  deformations and the boson Hamiltonian (5), the following wave function for the condensate state [77] of the  $s_\nu$ ,  $s_\pi$ ,  $d_\nu$ ,  $d_\pi$ ,  $f_\nu$ , and  $f_\pi$  bosons is considered:

$$|\Psi\rangle = \prod_{\rho=\nu,\pi} \frac{1}{\sqrt{n_\rho!}} (\lambda_\rho^\dagger)^{n_\rho} |0\rangle \quad (8)$$

with

$$\lambda_\rho^\dagger = s_\rho^\dagger + \tilde{\beta}_{2\rho} d_{\rho,0}^\dagger + \tilde{\beta}_{3\rho} f_{\rho,0}^\dagger, \quad (9)$$

and  $|0\rangle$  the boson vacuum, i.e., the inert core. The amplitudes  $\tilde{\beta}_{2\rho}$  and  $\tilde{\beta}_{3\rho}$  in (9) are boson analogs of the quadrupole  $\beta_2$  and octupole  $\beta_3$  deformations, respectively. The expectation value of the *sdf*-IBM-2 Hamiltonian gives energy surface of the boson system specified by the four variables  $\tilde{\beta}_{2\nu}$ ,  $\tilde{\beta}_{2\pi}$ ,  $\tilde{\beta}_{3\nu}$ , and  $\tilde{\beta}_{3\pi}$ . However, to treat the energy surface in the full four-dimensional space is practically so complicated that, in this study, it is assumed that the neutron and proton bosons should have the same deformations, i.e.,  $\tilde{\beta}_{2\nu} = \tilde{\beta}_{2\pi} \equiv \tilde{\beta}_2$  and  $\tilde{\beta}_{3\nu} = \tilde{\beta}_{3\pi} \equiv \tilde{\beta}_3$ . Under this assumption, the bosonic potential energy surface in the  $\tilde{\beta}_2 - \tilde{\beta}_3$  space is calculated as

$$\begin{aligned} \frac{\langle \Psi | \hat{H} | \Psi \rangle}{\langle \Psi | \Psi \rangle} &= \frac{(n_\nu + n_\pi)(\epsilon_d \tilde{\beta}_2^2 + \epsilon_f \tilde{\beta}_3^2)}{1 + \tilde{\beta}_2^2 + \tilde{\beta}_3^2} + \frac{n_\nu n_\pi}{(1 + \tilde{\beta}_2^2 + \tilde{\beta}_3^2)^2} \\ &\times \left[ \kappa_2 \left( 2\tilde{\beta}_2 - \sqrt{\frac{2}{7}} \chi_\nu \tilde{\beta}_2^2 - \frac{2}{\sqrt{21}} \chi'_\nu \tilde{\beta}_3^2 \right) \left( 2\tilde{\beta}_2 - \sqrt{\frac{2}{7}} \chi_\pi \tilde{\beta}_2^2 - \frac{2}{\sqrt{21}} \chi'_\pi \tilde{\beta}_3^2 \right) \right. \\ &\left. + \kappa_3 \left( 2\tilde{\beta}_3 - \frac{4}{\sqrt{15}} \chi''_\nu \tilde{\beta}_2 \tilde{\beta}_3 \right) \left( 2\tilde{\beta}_3 - \frac{4}{\sqrt{15}} \chi''_\pi \tilde{\beta}_2 \tilde{\beta}_3 \right) \right]. \quad (10) \end{aligned}$$

The strength parameters of the boson Hamiltonian (5) to be determined are  $\{\epsilon_d, \epsilon_f, \kappa_2, \chi_\nu, \chi_\pi, \chi'_\nu, \chi'_\pi, \kappa_3, \chi''_\nu, \chi''_\pi\}$ . To reduce the number of parameters, it is assumed that the dimensionless parameters  $\chi'_\nu$ ,  $\chi'_\pi$ ,  $\chi''_\nu$ , and  $\chi''_\pi$  are all equal,  $\chi'_\nu = \chi'_\pi = \chi''_\nu = \chi''_\pi \equiv \chi$ . It is further assumed that the bosonic deformation  $\tilde{\beta}_\lambda$  ( $\lambda = 2$  or  $3$ ) is proportional to the fermionic counterparts, i.e.,  $\tilde{\beta} \equiv C_\lambda \beta_\lambda$ .  $C_\lambda$  is a constant of proportionality, and is also determined by the procedure described below.

The seven parameters for the *sdf*-IBM-2 Hamiltonian, i.e.,  $\{\epsilon_d, \epsilon_f, \kappa_2, \chi_\nu, \chi_\pi, \kappa_3, \chi\}$  and the two constants  $C_2$  and  $C_3$ , are determined for each nucleus by mapping the

axially-symmetric  $\beta_2 - \beta_3$  SCMF potential energy surface onto the corresponding bosonic energy surface given by Eq. (10). Or equivalently, these strength parameters are fine tuned so that the *sdf*-IBM-2 energy surface of (10) becomes similar in topology to the SCMF one and that the approximate equality

$$E_{\text{SCMF}}(\beta_2, \beta_3) \approx E_{\text{IBM}}(\beta_2, \beta_3) \quad (11)$$

should be satisfied in the neighborhood of the global minimum. Limiting the range for the mapping (11) to the vicinity of the global mean-field minimum is due to the fact that in the SCMF framework, the configurations near the global minimum make the most relevant contri-

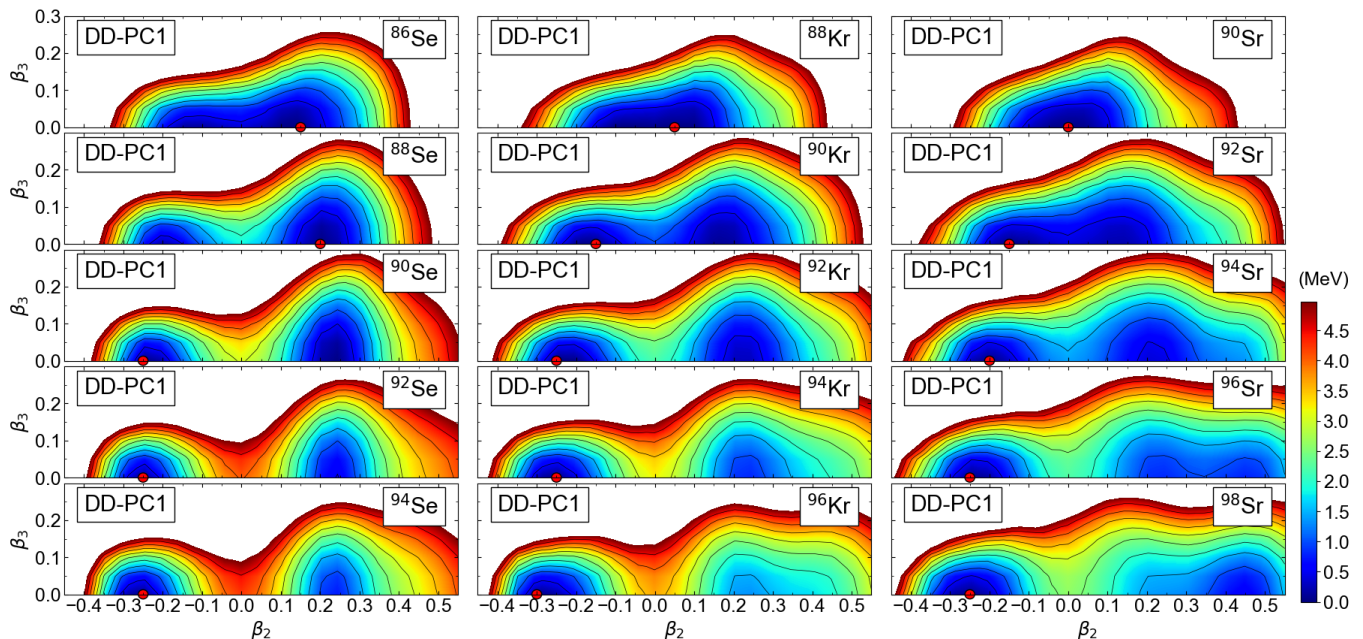


FIG. 1. Axially-symmetric quadrupole and octupole SCMF potential energy surfaces for the  $^{86-94}\text{Se}$ ,  $^{88-96}\text{Kr}$ , and  $^{90-98}\text{Sr}$  isotopes as functions of the  $\beta_2$  and  $\beta_3$  deformations, computed by the constrained RHB method with the DD-PC1 EDF and the separable pairing force of finite range. The energy difference between neighboring contours is 0.5 MeV, and the global minimum within the  $\beta_2 - \beta_3$  plane is indicated by the solid circle.

butions to determining the low-energy collective states. On the other hand, the regions very far from the minimum with large  $\beta_2$  and  $\beta_3$  deformations are more dominated by the quasiparticle degrees of freedom, which are by construction not taken into account in the present *sdf*-IBM-2 framework. For further details of the mapping procedure, the reader is referred to Refs. [48, 49, 78, 79].

Diagonalization of the mapped *sdf*-IBM-2 Hamiltonian with the strength parameters determined by the aforementioned procedure produces excitation spectra for both parities and electromagnetic transition rates. For the numerical diagonalization of the Hamiltonian, the computer program ARBMODEL [80] is used.

### III. RESULTS AND DISCUSSION

#### A. Potential energy surfaces

Figures 1 and 2 show contour plots of the axially-symmetric quadrupole and octupole deformation energy surfaces for the even-even nuclei  $^{86-94}\text{Se}$ ,  $^{88-96}\text{Kr}$ ,  $^{90-98}\text{Sr}$ ,  $^{92-100}\text{Zr}$ , and  $^{94-102}\text{Mo}$  as functions of the  $\beta_2$  and  $\beta_3$  deformations, computed by the constrained RHB method that is based on the DD-PC1 functional and the separable pairing force of finite range. For any of the nuclei under study, one finds no octupole deformed ground state minimum with  $\beta_3 \neq 0$  on the  $\beta_2 - \beta_3$  deformation energy surface. In general, however, the potential

appears to become rigid in the  $\beta_2$  deformation and softest along the  $\beta_3$  direction at the  $N = 56$  nucleus among each isotopic chain, the neutron number corresponding to the empirical octupole magic number. This feature is most notably observed in the Se isotopes, with their proton number  $Z = 34$  identified as the proton octupole magic number. For those nuclei with  $N > 56$  the energy surfaces become more rigid, especially in the  $\beta_3$  deformation, and the octupole correlations are expected to be less pronounced.

There are some other properties worth remarking of the SCMF energy surfaces. For the  $N = 52$  isotones, a nearly spherical minimum is suggested:  $\beta_2 \approx 0.05$  for  $^{86}\text{Se}$  and  $^{88}\text{Kr}$ , and  $\beta_2 \approx 0.0$  for  $^{90}\text{Sr}$ ,  $^{92}\text{Zr}$ , and  $^{94}\text{Mo}$ , the last three nuclei being in the immediate vicinity of the proton sub-shell closure  $Z = 40$ . All the  $N = 54$  isotones are here suggested to be soft in  $\beta_2$  deformation in the interval  $|\beta_2| \lesssim 0.2$ . In all the isotopic chains, the prolate-to-oblate shape transition is observed: in Figs. 1 and 2 a change in the location of the minimum from the prolate or nearly spherical to oblate sides at  $N = 54$  (Kr and Zr),  $N = 56$  (Se), and  $N = 58$  (Mo). In  $^{96,98}\text{Sr}$  and  $^{100}\text{Zr}$  another prolate minimum with quite a large  $\beta_2$  deformation ( $\beta_2 \gtrsim 0.4$ ) appears. These behaviours are considered a signature of the onset of intruder deformed configuration that is suggested to occur around the neutron number  $N = 60$ .

It can be also shown that the SCMF calculations with the reduced pairing strength  $V_0 = 728 \text{ MeV fm}^3$  produce the energy surfaces that are slightly steeper in both  $\beta_2$

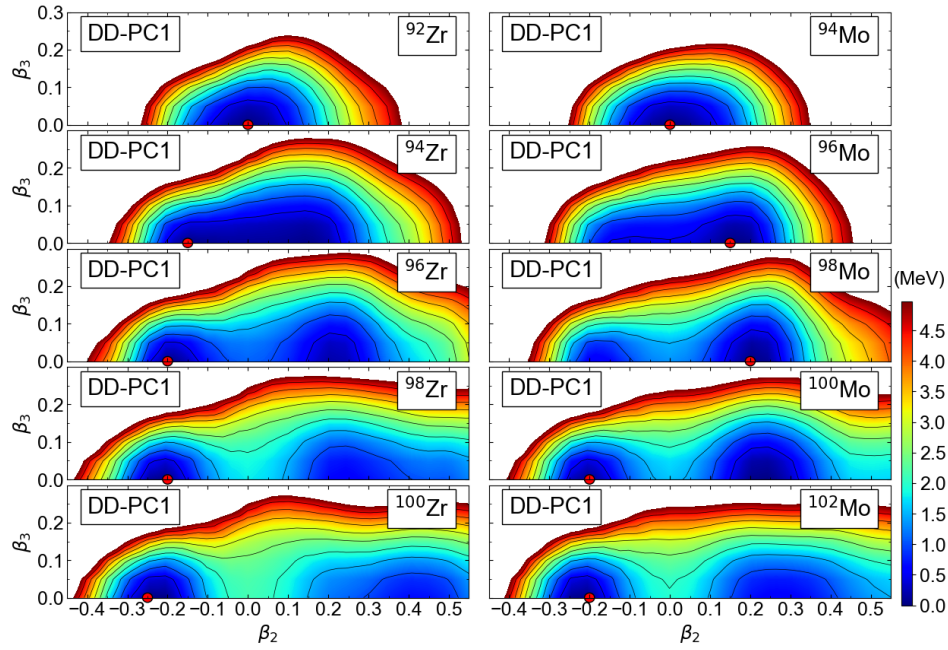


FIG. 2. Same as Fig. 1, but for the  $^{92-100}\text{Zr}$ , and  $^{94-102}\text{Mo}$  isotopes.

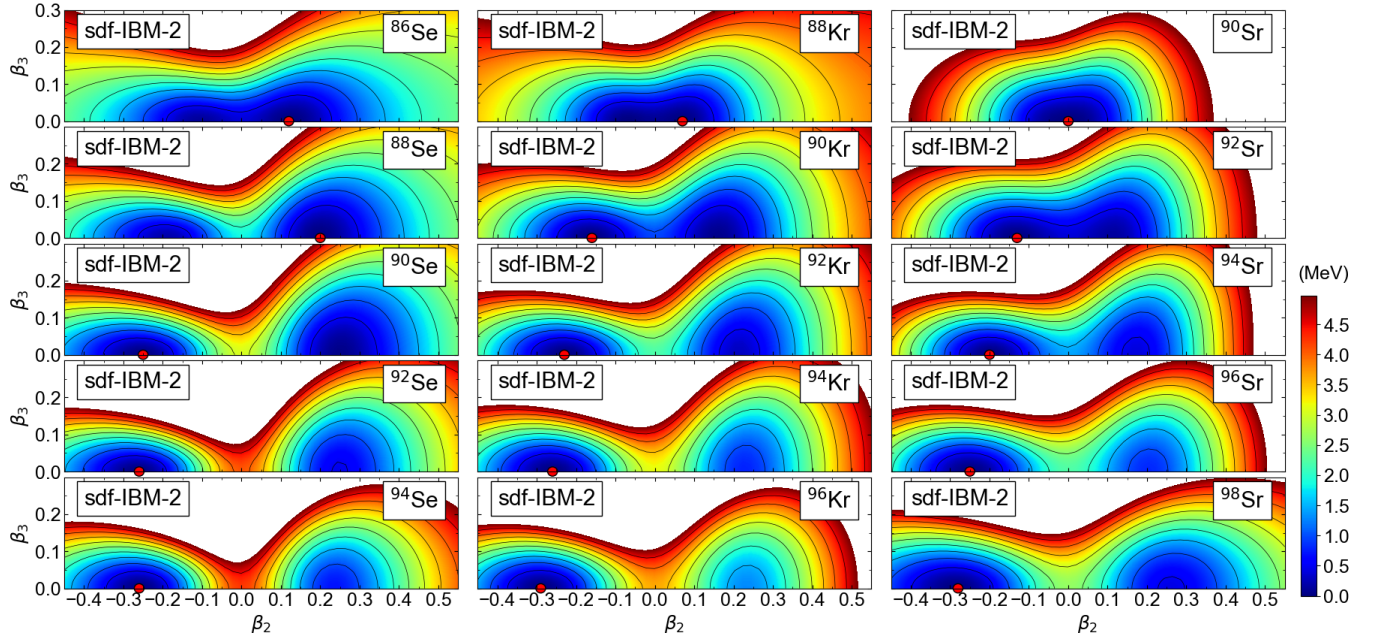


FIG. 3. Same as Fig. 1, but for the mapped *sdf*-IBM-2 potential energy surfaces for the  $^{86-94}\text{Se}$ ,  $^{88-96}\text{Kr}$ , and  $^{90-98}\text{Sr}$  isotopes.

and  $\beta_3$  deformations but that are qualitatively similar to the ones shown in Figs. 1 and 2, obtained with the increased pairing strength  $V_0 = 837 \text{ MeV fm}^3$ . In addition, the same constrained RHB calculations but employing the density-dependent meson-exchange (DD-ME2) functional [81], another representative effective interaction in the relativistic EDF framework, give strikingly similar

mean-field results to those in the case of the DD-PC1 EDF.

Figures 3 and 4 show the mapped *sdf*-IBM-2 potential energy surfaces. As compared to the SCMF energy surfaces in Figs. 1 and 2, one notices that the basic topology of the SCMF energy surface, up to typically 2 MeV excitation from the minimum, is reproduced by the

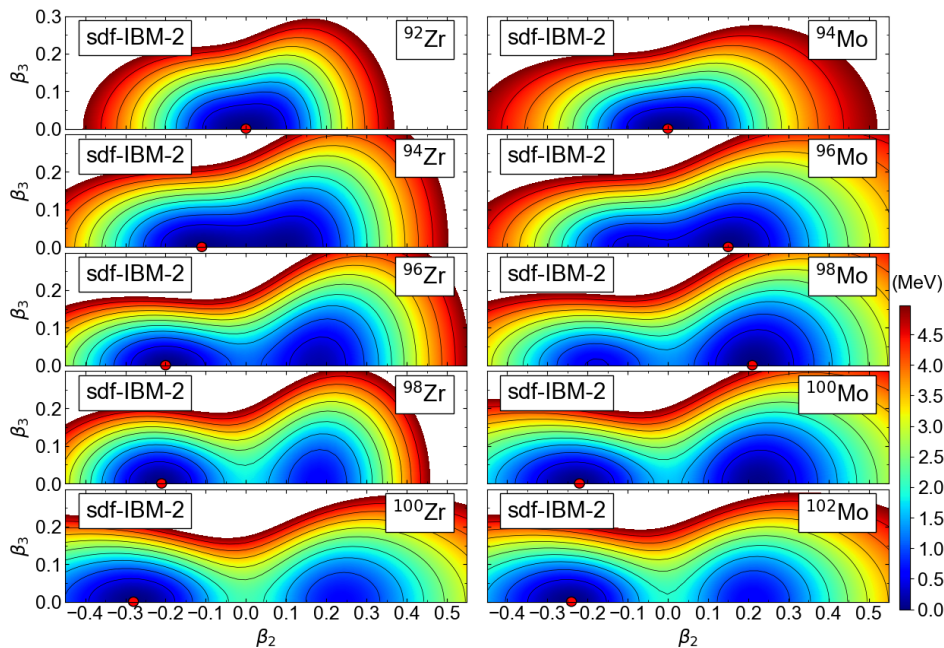


FIG. 4. Same as Fig. 4, but for the  $^{92-100}\text{Zr}$ , and  $^{94-102}\text{Mo}$  isotopes.

bosonic ones. One also finds that the *sdf*-IBM-2 energy surfaces are flat for higher excitation energies associated with large  $\beta_2$  and  $\beta_3$  deformations, in comparison to the SCMF counterparts. This difference illustrates that the *sdf*-IBM-2 space consists of only limited number of valence nucleons, while the SCMF model includes all nucleon degrees of freedom.

### B. Derived strength parameters

The derived *sdf*-IBM-2 strength parameters used for the spectroscopic calculations on the considered Se, Kr, Sr, Zr, and Mo nuclei are shown as functions of  $N$  in Fig. 5. In Fig. 5(a) one sees that the single-*d* boson energy  $\epsilon_d$  is mostly stable for  $52 \lesssim N \lesssim 58$ , but gradually decreases along the Mo chain. A sudden drop from  $N = 58$  to 60 in the derived  $\epsilon_d$  for the Sr and Zr isotopes is partly to account for the rapid structural change, i.e., onset of strong deformation, suggested empirically in these isotopic chains. The quadrupole-quadrupole interaction strength  $\kappa_2$  generally decreases in magnitude as the number of valence neutrons increases [cf. Fig. 5(b)]. The parameters  $\chi_\nu$  [Fig. 5(c)] and  $\chi_\pi$  [Fig. 5(d)] do not show any strong dependence on  $N$ , except for the  $\chi_\nu$  value for the Mo isotopes. The positive (negative) sign of the sum  $\chi_\nu + \chi_\pi$  determines whether a nucleus is oblate (prolate) deformed. In many of the considered nuclei, a weakly-deformed mean-field minimum occurs on the oblate side, hence the value of the sum  $\chi_\nu + \chi_\pi$  here has positive sign and small magnitude. The single *f*-boson energy  $\epsilon_f$  is here basically kept constant or made

only gradually change within the range  $2.7 \lesssim \epsilon_f \lesssim 3.0$ , while it significantly decreases with  $N$  for the Mo isotopic chain [Fig. 5(e)]. The value of the common parameter  $\chi (= \chi'_\nu = \chi'_\pi = \chi''_\nu = \chi''_\pi)$  in Fig. 5(f) is determined according to the degree of  $\beta_3$  softness of the potential. One sees that the derived  $\chi$  value is indeed large in magnitude for  $52 \lesssim N \lesssim 56$  as compared to those nuclei with  $N > 56$  for most of the studied isotopic chains. For the sake of simplicity, the octupole-octupole interaction strength  $\kappa_3 = 0.12$  MeV is here kept constant for all the nuclei.

### C. Systematics of low-energy spectra

Figure 6 compares the calculated low-energy spectra for the positive-parity even-spin states  $2_1^+$ ,  $4_1^+$ , and  $6_1^+$  of the considered nuclei with the experimental data [82]. One observes an overall reasonable agreement with the data, except perhaps for the Zr isotopes. For the Se, Kr, and Mo isotopes, both the theoretical and experimental energy levels are gradually lowered with the increasing  $N$ . The modest decrease of the calculated yrast spectra, from  $^{94}\text{Kr}$  to  $^{96}\text{Kr}$  in particular, suggests a smooth onset of deformation in agreement with the experiment [87]. For the Sr and Zr isotopic chains the present calculation gives a more rapid decrease of these states. One notices, in the corresponding experimental spectra in Figs. 6(c) and 6(d), a pronounced peak at the neutron number  $N = 56$ . This indicates the effect of the neutron  $N = 56$  sub-shell gap due to the filling in the  $\nu d_{5/2}$  orbital, which is even more enhanced for the Zr nuclei corresponding to the

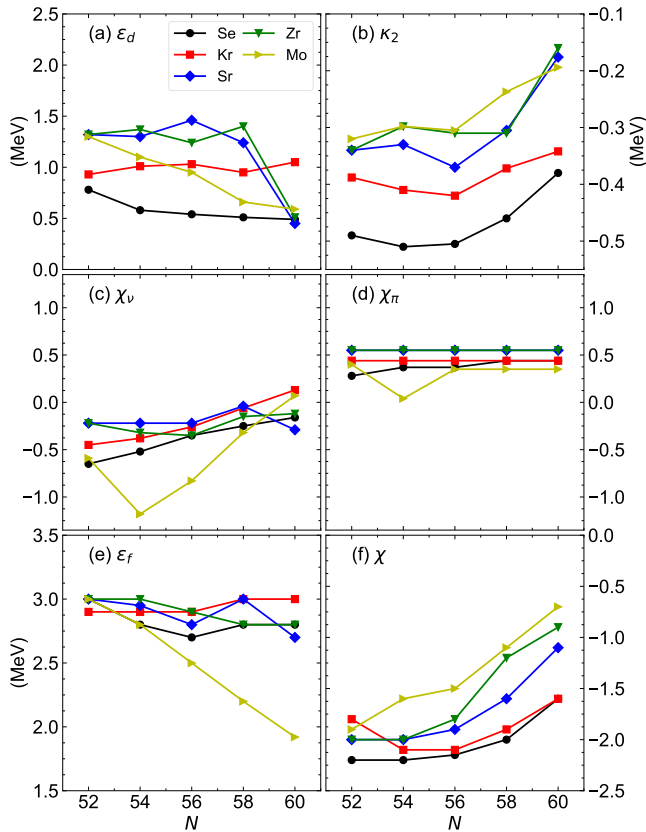


FIG. 5. Values of the parameters for the *sdf*-IBM-2 Hamiltonian. Note that  $\chi$  in panel (f) is defined as  $\chi = \chi'_\nu = \chi'_\pi = \chi''_\nu = \chi''_\pi$ . The octupole-octupole interaction strength  $\kappa_3$  is kept constant  $\kappa_3 = 0.12$  MeV, and is not shown.

proton sub-shell closure  $Z = 40$ . The mapped *sdf*-IBM-2 does not reproduce this trend in Zr, mainly because no spherical minimum occurs in the axially-symmetric quadrupole-octupole SCMF energy surface for  $^{96}\text{Zr}$  (cf. Fig. 2). The SCMF calculation gives for this nucleus only a weakly deformed oblate minimum at  $\beta_2 \approx -0.2$ , and consequently the mapped *sdf*-IBM-2 yields the collective energy spectrum, characterized by the low-lying  $2_1^+$  energy level and by the ratio of the  $4_1^+$  to  $2_1^+$  excitation energies  $R_{4/2} = 2.46$ . Another notable feature observed in the Sr and Zr isotopes is a sudden drop of the energy levels from  $N = 58$  to 60. The present calculation reproduces well this systematic. As for the  $N = 52$  isotones, the *sdf*-IBM-2 generally does not give a very good description, because these nuclei are close to the neutron  $N = 50$  major shell closure and the model space of the calculation including only one neutron boson may not be large enough to reproduce the positive-parity levels of the nearly spherical nuclei.

In Fig. 7, the calculated energy spectra for the low-lying negative-parity odd-spin states  $1_1^-$ ,  $3_1^-$ ,  $5_1^-$ , and  $7_1^-$  are shown as functions of  $N$ . Of particular interest regarding the predicted negative-parity energy spectra is

their parabolic dependence with  $N$  with the minimum values at  $N = 56$  for all the considered isotopic chains, except for Mo. This result is consistent with the systematic behaviour of the quadrupole-octupole potential energy surfaces, which exhibit the  $\beta_3$  softest potential for those nuclei with  $N \approx 56$ . As seen in Fig. 7, in accordance with the experimental data, the lowest negative-parity state is here predicted to be  $I = 3^-$  at the excitation energy  $E_x \approx 2$  MeV. Within the calculation, the  $1^-$  energy level is rather high and is close to the  $5_1^-$  one. This level structure is at variance with the ones observed, e.g., in the actinide nuclei with  $N \approx 134$ . In the latter mass region, the lowest negative-parity state in many cases is the  $1^-$  state, upon which an approximate alternating-parity rotational band develops. One may notice that the predicted higher-spin negative-parity states, especially the  $7_1^-$  one, is higher than the experimental value, most notably, for  $^{94,96}\text{Se}$  and  $^{94}\text{Kr}$ . It is noted, however, that the observed low-lying  $7^-$  state in these nuclei could be attributed to isomeric state based on the neutron two-quasiparticle excitations (see, e.g., Ref. [86]), which are not considered in the present *sdf*-IBM-2 model space.

#### D. *f*-boson contributions to wave functions

To interpret the nature of the low-lying states, contributions of the *f* bosons to the corresponding *sdf*-IBM-2 wave functions are studied. As an illustrative example, Fig. 8 shows the expectation values of the neutron  $\hat{n}_{f_\nu}$  and proton  $\hat{n}_{f_\pi}$  boson number operators calculated by using the wave functions for the low-spin positive-parity states  $0_1^+$ ,  $2_1^+$ ,  $0_2^+$ , and  $2_2^+$ , and negative-parity states  $1_1^-$ , and  $3_1^-$ . As one can see in panels (a) to (d) and (g) to (j) of Fig. 8, there is only a small admixture of the  $f_\nu$  and  $f_\pi$  bosons into the low-energy positive-parity states, with the expectation value  $\hat{n}_{f_\rho}$  typically  $\langle \hat{n}_{f_\rho} \rangle \lesssim 0.2$ . In the  $0_2^+$  wave functions there appears to be a relatively large *f*-boson contributions at  $N = 56$ , in particular, for  $^{90}\text{Se}$ ,  $^{92}\text{Kr}$  and  $^{94}\text{Sr}$ , in which nuclei the octupole correlations are expected to be most pronounced. For the negative-parity states  $1_1^-$  and  $3_1^-$ , the calculated expectation value  $\langle \hat{n}_{f_\rho} \rangle \approx 0.5$  for both proton and neutron bosons, and hence  $\langle \hat{n}_{f_\rho} + \hat{n}_{f_\nu} \rangle \approx 1$ . Therefore, the wave functions for the above negative-parity states contain approximately one-*f* boson components.

#### E. Electromagnetic transition properties

Electromagnetic properties considered in this paper are those of the electric quadrupole  $E2$ , octupole  $E3$ , dipole  $E1$ , and magnetic dipole  $M1$  transitions. The cor-

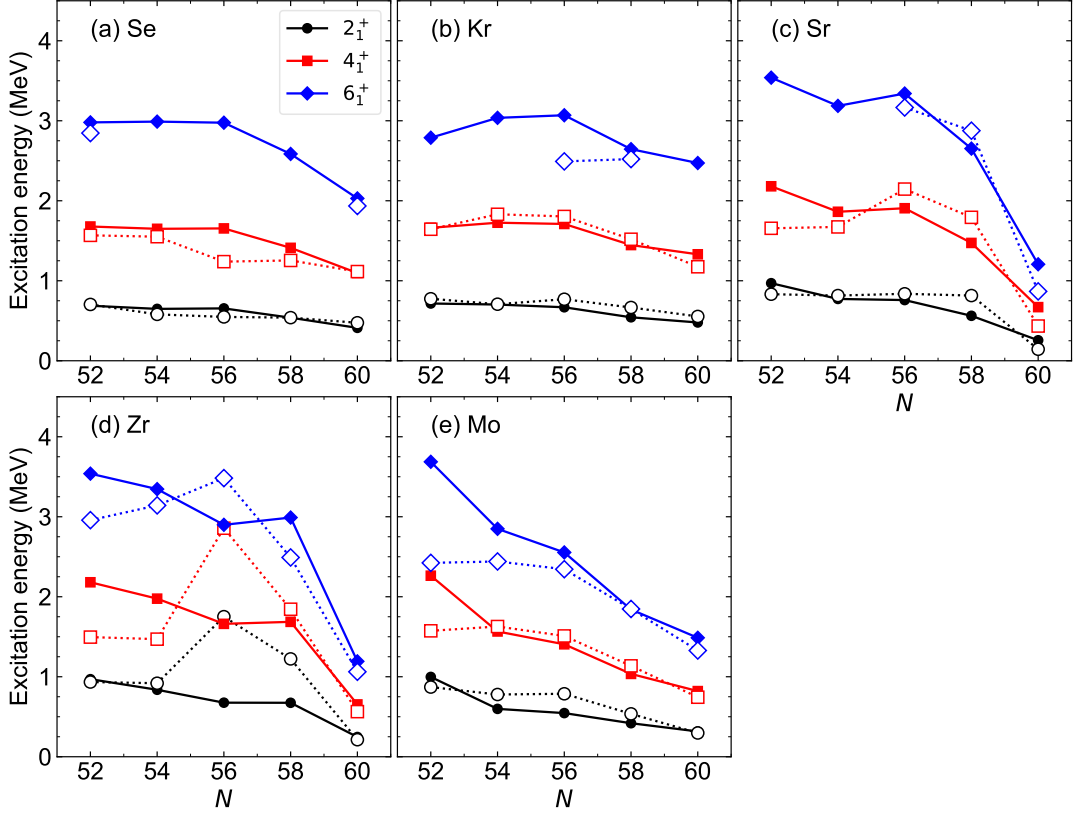


FIG. 6. Low-energy spectra for positive-parity even-spin states  $2_1^+$ ,  $4_1^+$ , and  $6_1^+$  of the considered even-even nuclei  $^{86-94}\text{Se}$ ,  $^{88-96}\text{Kr}$ ,  $^{90-98}\text{Sr}$ ,  $^{92-100}\text{Zr}$ , and  $^{94-102}\text{Mo}$ . Theoretical and experimental values are represented by the solid and open symbols, which are connected by the solid and dotted lines, respectively. The experimental data are taken from Refs. [9, 10, 16, 82–86].

responding operators are:

$$\hat{T}^{(E2)} = \sum_{\rho=\nu,\pi} e_{2,\rho} \hat{Q}_\rho, \quad (12)$$

$$\hat{T}^{(E3)} = \sum_{\rho=\nu,\pi} e_{3,\rho} \hat{O}_\rho, \quad (13)$$

$$\hat{T}^{(E1)} = \sum_{\rho=\nu,\pi} e_{1,\rho} \hat{D}_\rho, \quad (14)$$

$$\hat{T}^{(M1)} = \sqrt{\frac{3}{4\pi}} \sum_{\rho=\nu,\pi} g_\rho \hat{L}_\rho, \quad (15)$$

where the operators  $\hat{Q}_\rho$  and  $\hat{O}_\rho$  are the same quadrupole and octupole operators as in the Hamiltonian (5) with the same values of the parameters  $\chi_\rho$ ,  $\chi'_\rho$ , and  $\chi''_\rho$ , and

$$\hat{D}_\rho = (d_\rho^\dagger \times \tilde{f}_\rho + f_\rho^\dagger \times \tilde{d}_\rho)^{(1)} \quad (16)$$

$$\hat{L}_\rho = \sqrt{10}(d_\rho^\dagger \times \tilde{d}_\rho)^{(1)} + \sqrt{28}(f_\rho^\dagger \times \tilde{f}_\rho)^{(1)} \quad (17)$$

are electric and magnetic dipole transition operators, respectively.  $e_{\lambda,\rho}$  ( $\lambda = 1, 2, 3$ ) in Eqs. (12)–(14) are effective boson charges, and  $g_\rho$  in (15) is the bosonic gyromagnetic ( $g$ ) factor. The neutron and proton effective

charges are assumed to be equal, i.e.,  $e_{1,\nu} = e_{1,\pi} \equiv e_1$ ,  $e_{2,\nu} = e_{2,\pi} \equiv e_2$ , and  $e_{3,\nu} = e_{3,\pi} \equiv e_3$ , and the fixed effective charges  $e_1 = 0.005 \text{ eb}^{1/2}$ ,  $e_2 = 0.06 \text{ eb}$ , and  $e_3 = 0.06 \text{ eb}^{3/2}$  are used so as to reasonably reproduce the experimental data. The empirical boson  $g$  factors  $g_\nu = 0 \mu_N$  and  $g_\pi = 1 \mu_N$  are adopted by following the microscopic calculations in the previous ( $sd$ )-IBM-2 studies [92].

Systematic behaviours of the reduced  $E2$ ,  $E3$ , and  $E1$  transition probabilities between the lowest positive- and negative-parity states,  $B(E2; 2_1^+ \rightarrow 0_1^+)$ ,  $B(E3; 3_1^- \rightarrow 0_1^+)$ , and  $B(E1; 3_1^- \rightarrow 2_1^+)$ , are shown in Fig. 9. Results for the  $M1$  properties are discussed in the next section for individual nuclei. Both the calculated and experimental  $2_1^+ \rightarrow 0_1^+$   $E2$  transition rates are weak for  $52 \leq N \leq 58$ , with the  $B(E2)$  values typically lower than 20 Weisskopf units (W.u.). The experimental data show a significant rise of the  $B(E2; 2_1^+ \rightarrow 0_1^+)$  values from  $N = 58$  to 60 in the Sr, Zr, and Mo isotopes, as a consequence of the strong quadrupole deformation setting in.

The  $B(E3; 3_1^- \rightarrow 0_1^+)$  rates are a direct measure of the octupole collectivity, and are generally large for those nuclei that are expected to have an enhanced octupole deformation. Experimental data for the  $B(E3; 3_1^- \rightarrow 0_1^+)$  rates are available [13, 15, 88] for Zr and Mo nuclei. One

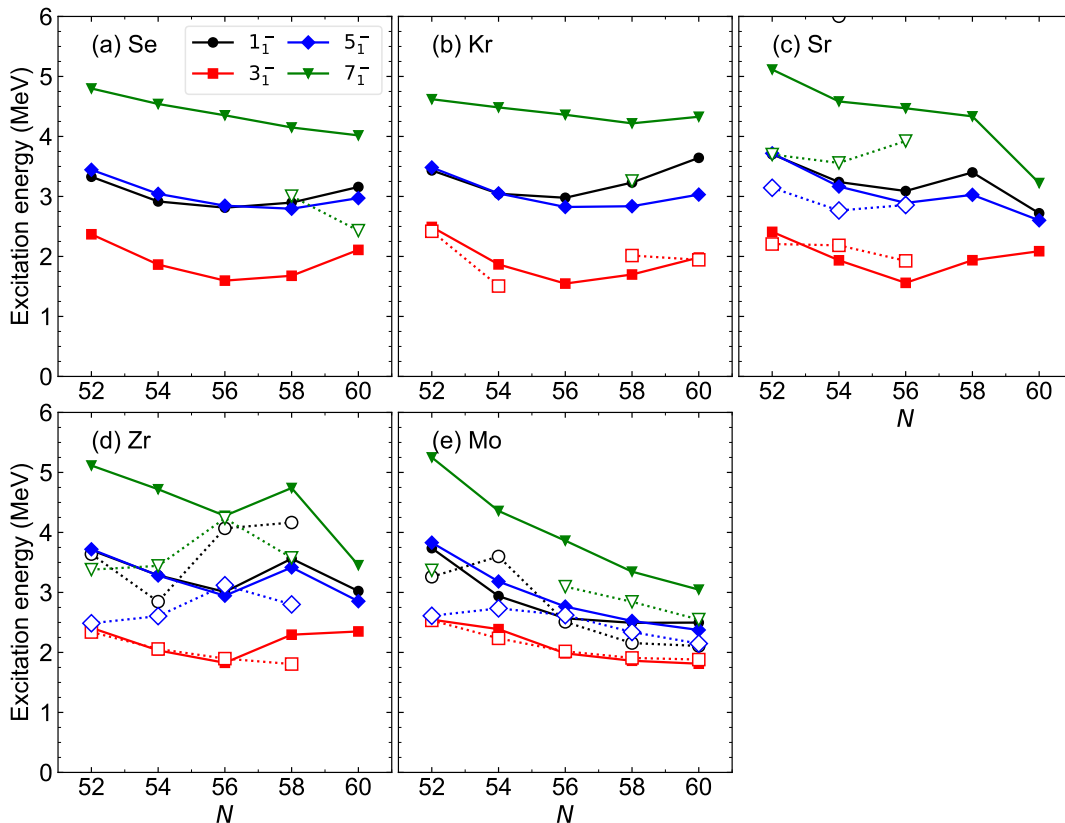


FIG. 7. Same as Fig. 6, but for negative-parity odd-spin states  $1_1^-$ ,  $3_1^-$ ,  $5_1^-$ , and  $7_1^-$ .

finds in Fig. 9(d) that experimental  $B(E3; 3_1^- \rightarrow 0_1^+)$  value is particularly large for  $^{96}\text{Zr}$ ,  $57 \pm 4$  W.u., and slowly increases toward the middle of the neutron major shell in the Mo isotopes. The  $B(E3; 3_1^- \rightarrow 0_1^+)$  rates predicted by the *sdf*-IBM-2 calculation are within the range  $\approx 20 - 30$  W.u. for all the studied isotopic chains. Note, however, that the calculated values for the Zr and Mo chains are virtually constant against  $N$ , being at variance with the observed systematic.

The  $B(E1; 3_1^- \rightarrow 2_1^+)$  transition rate is also a relevant quantity to the octupole deformation. There are some data available. Especially, recent measurements for  $^{94}\text{Kr}$  and  $^{96}\text{Kr}$  suggested the 1350 and 1390 keV decays, respectively, of the  $3^-$  to  $2_1^+$  states [16]. The calculated  $B(E1; 3_1^- \rightarrow 2_1^+)$  values shown in Fig. 9(e) are large near the neutron  $N = 50$  major shell gap, and decrease rather rapidly with  $N$  toward  $N = 60$ . The measured  $B(E1; 3_1^- \rightarrow 2_1^+)$  values seem to be quite different from one isotopic chain to another, whereas the present calculation gives rather similar values and systematic behaviours among the five isotopic chains. One should also note that, since the  $E1$  mode is more of single-particle nature than the  $E2$  and  $E3$  ones, the *sdf*-IBM descriptions in general, which consist only of collective degrees of freedom, may not give meaningful predictions for the  $E1$  transition properties. A more reliable IBM description

of the  $E1$  transition properties could include the dipole  $p$  bosons with  $J = 1^-$  as additional degrees of freedom to the boson model space [40–42]. This extension, however, lies beyond the scope of the present theoretical analysis.

## F. Low-energy spectra for Kr nuclei

Figures 10, 11, and 12 show detailed low-energy spectra for the neutron-rich isotopes  $^{92}\text{Kr}$ ,  $^{94}\text{Kr}$ , and  $^{96}\text{Kr}$ , respectively. The positive-parity part of the level scheme consist of the states in the  $K = 0_1^+$  ground-state band and states not classified into bands. For the negative-parity part only the spectra for the odd-spin states are shown.

The  $^{92}\text{Kr}$  nucleus corresponds to the octupole neutron magic number  $N = 56$ , and the corresponding  $\beta_2 - \beta_3$  potential energy surface is soft in  $\beta_3$  deformation (cf. Figs. 1 and 3). As one sees in Fig. 10, the calculation reproduces well the observed  $K = 0_1^+$  band, and predicts the  $2_2^+$  states near the  $4_1^+$  state, which is considered as the bandhead of the quasi- $\gamma$  or  $K = 2_2^+$  band that comprises the  $4_2^+$ ,  $3_1^+$ , and  $5_1^+$  states. The near degeneracy of the  $\gamma$ -band members, i.e.,  $3_1^+$  and  $4_2^+$ , indicates the O(6)-like level structure [92]. The  $0_2^+$  and  $2_3^+$  states predicted by the calculation are part of the  $K = 0_2^+$  band.

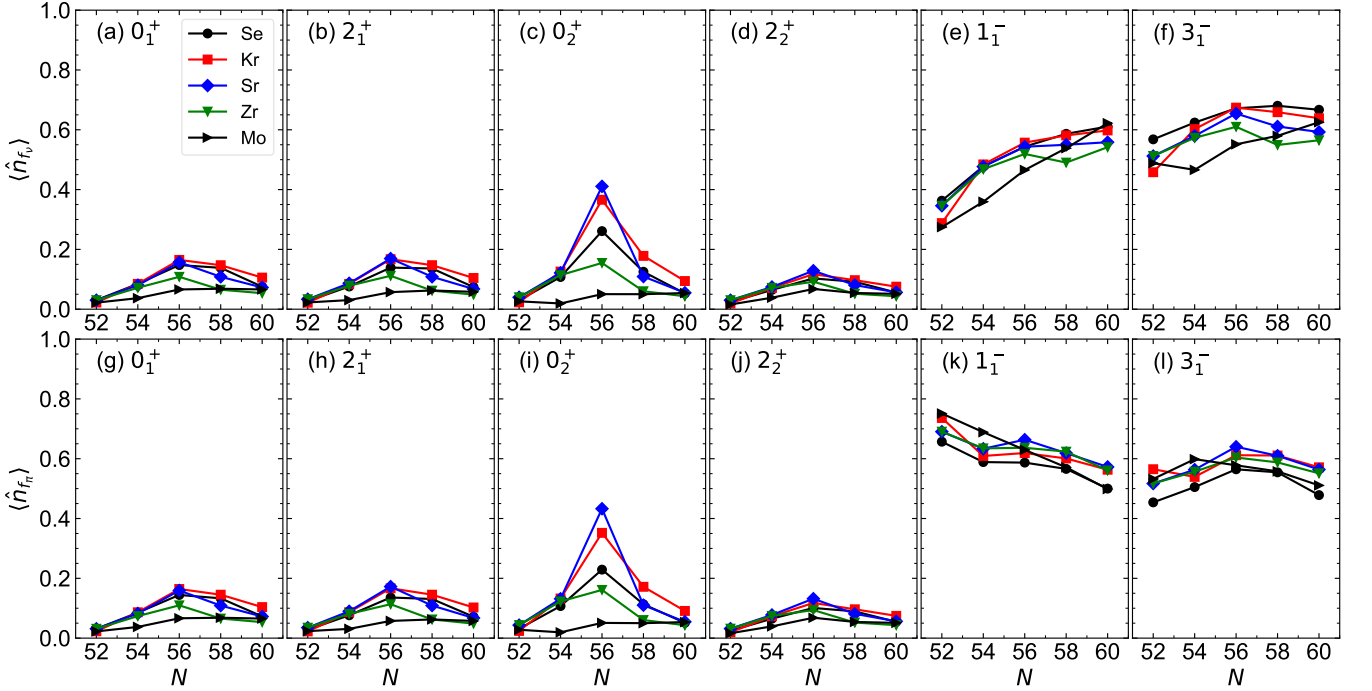


FIG. 8. Expectation values of neutron  $\hat{n}_{f\nu}$  (upper row) and proton  $\hat{n}_{f\pi}$  (lower row) number operators calculated for the  $0_1^+$  [panels (a) and (g)],  $2_1^+$  [(b) and (h)],  $0_2^+$  [(c) and (i)],  $2_2^+$  [(d) and (j)],  $1_1^-$  [(e) and (k)], and  $3_1^-$  [(f) and (l)] states for the considered Se, Kr, Sr, Zr, and Mo nuclei.

The mapped *sdf*-IBM-2 gives the low-lying  $3_1^-$  state at around the excitation energy  $E_x = 1.5$  MeV, below the  $4_1^+$  state. Remember that, among the considered Kr isotopes, the lowest  $3_1^-$  level is obtained for  $^{92}\text{Kr}$  in the present calculation [cf. Fig. 7(b)].

Similar results to  $^{92}\text{Kr}$  are obtained for the  $^{94}\text{Kr}$  (Fig. 11) and  $^{96}\text{Kr}$  (Fig. 12). In these two nuclei, the *sdf*-IBM-2 energy spectra for the  $K = 0_1^+$  band looks rather rotational as compared to the experimental counterparts, such that the calculated  $2_1^+$  energy level is more compressed. The calculated spectra for the positive-parity non-yrast bands in  $^{94,96}\text{Kr}$  are also rather high with respect to the  $K = 0_1^+$  band, and especially for  $^{96}\text{Kr}$ , overestimate the corresponding observed non-yrast levels. The calculated  $3_1^-$  excitation energies for both  $^{94}\text{Kr}$  and  $^{96}\text{Kr}$  are, however, in a good agreement with the experimental values [16], 2015 keV and 1944 keV, respectively.

Table I lists the predicted  $B(E2)$ ,  $B(M1)$ ,  $B(E1)$ , and  $B(E3)$  transition strengths, and electric quadrupole  $Q(I)$  and magnetic dipole  $\mu(I)$  moments for the  $^{92,94,96}\text{Kr}$  isotopes. One can see from the table that the calculated values for these electromagnetic properties are basically similar among the three Kr nuclei. The inband  $\Delta I = 2$   $E2$  transitions, i.e.,  $2_1^+ \rightarrow 0_1^+$ ,  $4_1^+ \rightarrow 2_1^+$ ,  $6_1^+ \rightarrow 4_1^+$ ,  $5_1^- \rightarrow 3_1^-$ , and  $7_1^- \rightarrow 5_1^-$ , as well as the  $Q(2_1^+)$  values, gradually increase from  $^{92}\text{Kr}$  to  $^{96}\text{Kr}$ . These systematics illustrate gradual evolution of quadrupole collectivity. The avail-

able experimental data [90],  $B(E2; 2_1^+ \rightarrow 0_1^+) = 13.6_{-3.3}^{+2.8}$  W.u.,  $19.5_{-2.1}^{+2.2}$  W.u., and  $33.4_{-6.7}^{+7.4}$  W.u. for  $^{92}\text{Kr}$ ,  $^{94}\text{Kr}$ , and  $^{96}\text{Kr}$ , respectively, are reasonably reproduced by the present *sdf*-IBM-2 calculation. The data also available from Ref. [90] for the  $Q(2_1^+)$  values,  $-0.61_{-0.45}^{+0.53}$  eb and  $-0.26_{-0.16}^{+0.19}$  eb, for  $^{92}\text{Kr}$  and  $^{94}\text{Kr}$ , respectively, are rather at variance with the present theoretical values both in sign and magnitude. The calculated  $Q(2_1^+)$  value for  $^{96}\text{Kr}$  is, however, within error bar of the experimental one [90],  $0.15 \pm 0.53$  eb. The considered  $B(E3)$  values also become gradually larger for heavier Kr as the neutron number increases. This is a consequence of the fact that almost constant strength parameters are used for the Kr isotopes (cf. Fig. 5), and thus these transition rates increase only monotonously with the boson number.

For completeness, Table I shows some calculated  $B(M1)$  and  $B(E1)$  dipole transitions. An interesting feature is that the calculated  $B(M1; 3_2^- \rightarrow 3_1^-)$  transition rate is large  $\gtrsim 0.01$  W.u., while the corresponding  $B(E2)$  value  $B(E2; 3_2^- \rightarrow 3_1^-) < 1$  W.u. is small. Experimentally, strong  $M1$  transitions from the  $3_i^-$  ( $i = 1$  or  $2$ ) excited state at  $E_x \approx 3.1$  MeV to the  $3_1^-$  state have been suggested in some of the nearly spherical  $N = 52$  isotones  $^{92}\text{Zr}$  and  $^{94,96}\text{Mo}$  [11], and have been identified as the isovector octupole excitation modes. As for the  $B(E1)$  rates, the transitions from the higher-spin negative-parity to lower-spin positive-parity states are systematically larger than those in the opposite direc-

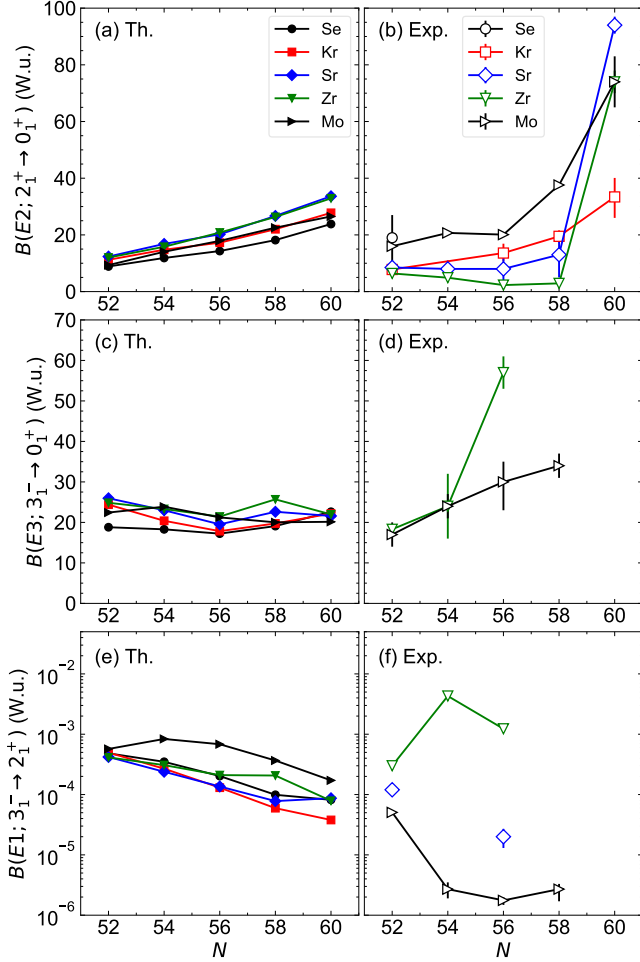


FIG. 9. Evolution of calculated and experimental  $B(E2; 2_1^+ \rightarrow 0_1^+)$  [(a) and (b)],  $B(E3; 3_1^- \rightarrow 0_1^+)$  [(c) and (d)], and  $B(E1; 3_1^- \rightarrow 2_1^+)$  [(e) and (f)] transition strengths in Weisskopf units (W.u.) for the Se, Kr, Sr, Zr, and Mo isotopes with  $52 \leq N \leq 60$ . The experimental data are adopted from Refs. [13, 15, 82, 88–91]. Note that a lower limit is shown for the experimental  $B(E1)$  value for  $^{90}\text{Sr}$  in panel (f).

tion, i.e., from the lower-spin negative-parity to higher-spin positive-parity states. Similar tendency has been obtained in the previous *sdf*-IBM calculations in other mass regions [45, 49], and this staggering pattern in the  $B(E1)$  rates can be partly attributed to the fact that the model space and the  $E1$  transition operator do not include the effect of  $p$ -boson degree of freedom. At any rate, experimental data on the transition properties is so scarce for the neutron-rich Kr isotopes that an extensive assessments of the model description and of the quality of the *sdf*-IBM-2 wave functions remain to be done.

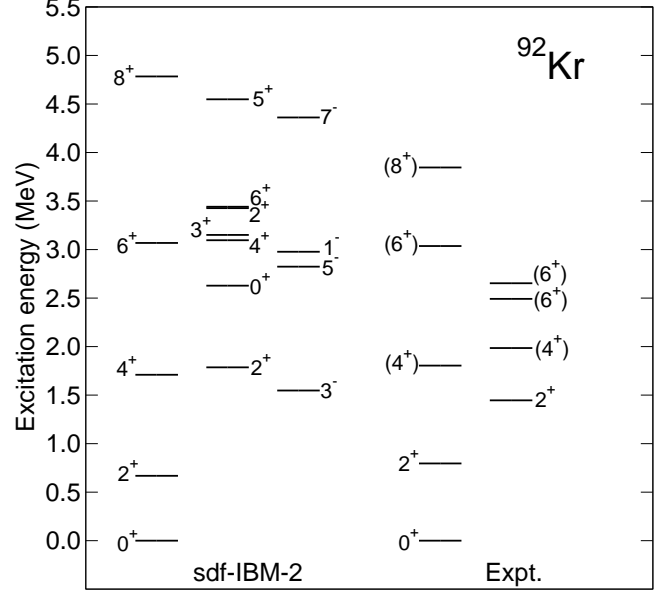


FIG. 10. Predicted and experimental low-energy positive- and negative-parity spectra for  $^{92}\text{Kr}$ . The experimental data are taken from Ref. [12].

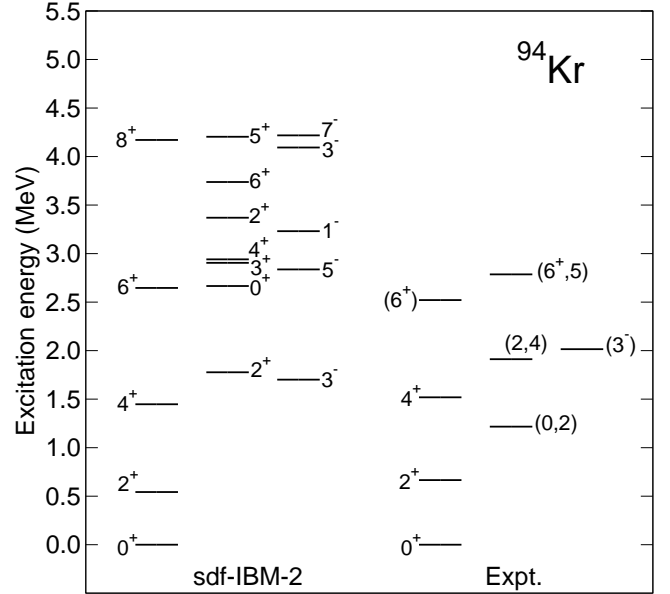


FIG. 11. Same as Fig. 10, but for  $^{94}\text{Kr}$ . The experimental data are taken from Ref. [16].

### G. Low-energy spectra for $N = 56$ isotones

Figure 13 shows the low-energy level schemes for the  $N = 56$  isotones other than  $^{92}\text{Kr}$ , that is,  $^{90}\text{Se}$ ,  $^{94}\text{Sr}$ ,  $^{96}\text{Zr}$ , and  $^{98}\text{Mo}$ .

The nucleus  $^{90}\text{Se}$  corresponds to both the neutron  $N = 56$  and proton  $Z = 34$  empirical octupole magic

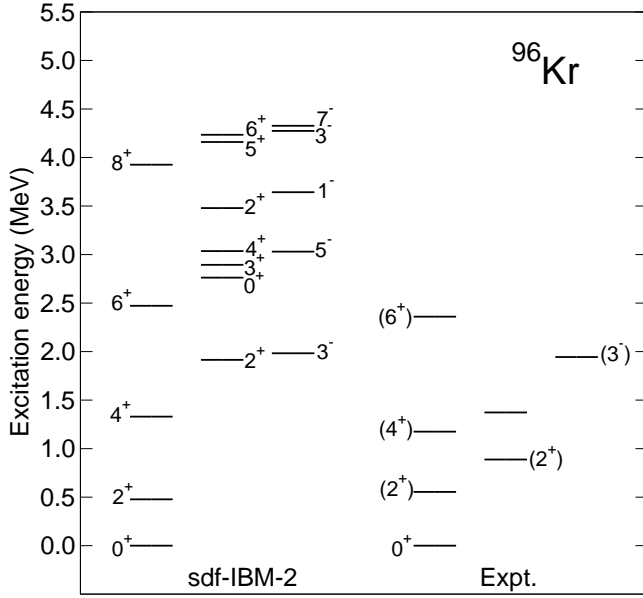


FIG. 12. Same as Fig. 10, but for  $^{96}\text{Kr}$ . The experimental data are taken from Ref. [16].

numbers. The SCMF result for this nucleus suggests that it is significantly soft in the octupole  $\beta_3$  deformation (see, Fig. 1). The predicted low-energy spectrum in Fig. 13 for  $^{90}\text{Se}$  resembles the one for the neighboring isotone  $^{92}\text{Kr}$ . For instance, the  $4_1^+$ ,  $2_2^+$ , and  $3_1^-$  states are nearly degenerated at  $E_x \approx 1.5$  MeV. In addition, the calculation predicts the  $3_1^-$  excitation energy to be  $E_x = 1597$  keV, while, experimentally [84], there is a level at  $E_x = 1600$  keV with tentatively assigned spin and parity  $(3, 4^+)$ . As compared to the experimental [84] energy spectrum, the predicted  $K = 0_1^+$  band is rather stretched. Some calculated  $B(E2)$ ,  $B(M1)$ ,  $B(E1)$ , and  $B(E3)$  transition rates and the  $Q(I)$  and  $\mu(I)$  moments are listed in Table II. Note that the experimental data for the electromagnetic transition properties are not available for this nucleus.

For  $^{94}\text{Sr}$ , an agreement between the *sdf*-IBM-2 and the experimental [82, 83] low-energy spectra is generally satisfactory, particularly for the  $K = 0_1^+$  band, the bandhead energy of the quasi- $\gamma$  band  $2_2^+$ , and many of the negative-parity states. A particularly low energy  $6_2^+$  state, almost degenerated with the  $6_1^+$  one, arises probably because a large fraction of the  $f$ -boson components is contained in its wave function. The calculation gives the low-lying  $3_1^-$  state below the  $4_1^+$  state, and also reproduces the even-spin negative-parity states  $4^-$  and  $6^-$ . The predicted  $3_2^-$  energy is, however, much higher than the experimental one. Note that the spin and parity of the  $3_1^-$  and  $3_2^-$  states are not firmly established experimentally. Predicted  $B(E2)$ ,  $B(M1)$ ,  $B(E1)$ , and  $B(E3)$  transition rates and the  $Q(I)$  and  $\mu(I)$  moments for  $^{94}\text{Sr}$  are summarized in Table II. The available experimental data [82] are:  $B(E2; 2_1^+ \rightarrow 0_1^+) = 8 \pm 4$  W.u.,  $B(E1; 3_2^- \rightarrow 2_1^+) = (2.0 \pm 0.7) \times 10^{-5}$  W.u., and

TABLE I. Calculated  $B(E2)$ ,  $B(M1)$ ,  $B(E3)$ , and  $B(E1)$  values (in W.u.), and electric quadrupole  $Q(I)$  (in eb) and magnetic dipole  $\mu(I)$  (in  $\mu_N$ ) moments for  $^{92,94,96}\text{Kr}$ .

	$^{92}\text{Kr}$	$^{94}\text{Kr}$	$^{96}\text{Kr}$
$B(E2; 2_1^+ \rightarrow 0_1^+)$	17	22	28
$B(E2; 4_1^+ \rightarrow 2_1^+)$	24	31	40
$B(E2; 6_1^+ \rightarrow 4_1^+)$	25	34	43
$B(E2; 0_2^+ \rightarrow 2_1^+)$	0.021	0.46	2
$B(E2; 0_2^+ \rightarrow 2_2^+)$	19	29	32
$B(E2; 2_2^+ \rightarrow 2_1^+)$	19	16	14
$B(E2; 3_1^+ \rightarrow 2_2^+)$	18	23	30
$B(E2; 4_2^+ \rightarrow 2_1^+)$	0.11	0.08	0.084
$B(E2; 4_2^+ \rightarrow 2_2^+)$	14	18	22
$B(E2; 4_2^+ \rightarrow 3_1^+)$	1.5	4.6	10
$B(E2; 4_2^+ \rightarrow 4_1^+)$	10	10	9.9
$B(E2; 3_2^- \rightarrow 3_1^-)$	0.16	0.036	0.011
$B(E2; 5_1^- \rightarrow 3_1^-)$	7.2	8.5	11
$B(E2; 7_1^- \rightarrow 5_1^-)$	12	15	21
$B(E2; 9_1^- \rightarrow 7_1^-)$	0.031	18	25
$B(M1; 2_2^+ \rightarrow 2_1^+)$	0.00046	0.00028	0.00015
$B(M1; 3_1^+ \rightarrow 2_2^+)$	0.00086	0.0004	0.00032
$B(M1; 4_2^+ \rightarrow 4_1^+)$	0.0018	0.0011	0.0006
$B(M1; 4_2^+ \rightarrow 3_1^+)$	$1.8 \times 10^{-5}$	$9.7 \times 10^{-6}$	$6.0 \times 10^{-5}$
$B(M1; 3_2^- \rightarrow 3_1^-)$	0.015	0.011	0.011
$B(E1; 1_1^- \rightarrow 0_1^+)$	$7.8 \times 10^{-5}$	$7.6 \times 10^{-5}$	$9.9 \times 10^{-5}$
$B(E1; 1_1^- \rightarrow 2_1^+)$	$1.0 \times 10^{-5}$	$6.9 \times 10^{-6}$	$3.4 \times 10^{-6}$
$B(E1; 3_1^- \rightarrow 2_1^+)$	$1.3 \times 10^{-4}$	$5.9 \times 10^{-5}$	$3.8 \times 10^{-5}$
$B(E1; 3_1^- \rightarrow 4_1^+)$	$1.2 \times 10^{-7}$	$5.1 \times 10^{-7}$	$1.0 \times 10^{-6}$
$B(E1; 5_1^- \rightarrow 4_1^+)$	$3.7 \times 10^{-4}$	$2.1 \times 10^{-4}$	$1.6 \times 10^{-4}$
$B(E1; 5_1^- \rightarrow 6_1^+)$	$1.0 \times 10^{-6}$	$1.3 \times 10^{-6}$	$4.3 \times 10^{-6}$
$B(E1; 7_1^- \rightarrow 6_1^+)$	$7.9 \times 10^{-4}$	$5.3 \times 10^{-4}$	$4.5 \times 10^{-4}$
$B(E3; 3_1^- \rightarrow 0_1^+)$	18	20	22
$B(E3; 3_1^- \rightarrow 2_1^+)$	41	43	44
$B(E3; 5_1^- \rightarrow 2_1^+)$	11	10	11
$B(E3; 5_1^- \rightarrow 4_1^+)$	34	39	42
$B(E3; 7_1^- \rightarrow 4_1^+)$	9.8	8.6	9.9
$B(E3; 7_1^- \rightarrow 6_1^+)$	29	34	37
$Q(2_1^+)$	0.19	0.34	0.45
$\mu(2_1^+)$	0.37	0.32	0.32

$$B(E1; 5_1^- \rightarrow 4_1^+) = (1.5 \pm 0.7) \times 10^{-5} \text{ W.u.}$$

The  $^{96}\text{Zr}$  nucleus corresponds to the doubly sub-shell closure of  $N = 56$  and  $Z = 40$ . As already shown in Fig. 6(d), the *sdf*-IBM-2 only produces a collective band structure for the positive-parity yrast band, whereas experimentally [91], the first excited state is the  $0_2^+$  state at  $E_x = 1582$  keV and the high-lying  $2_1^+$  state is found at 1750 keV. It was shown by the Monte-Carlo Shell Model calculation [91, 94] that this  $0_2^+$  is likely to arise from the intruder deformed configuration. The  $0_2^+$  state obtained by the present *sdf*-IBM-2 calculation is quite different in nature, since in the present framework the intruder excitations and the subsequent configuration mixing between the normal and intruder states are not taken into account. As for the negative-parity states, however, the mapped *sdf*-IBM-2 calculation generally provides a rea-

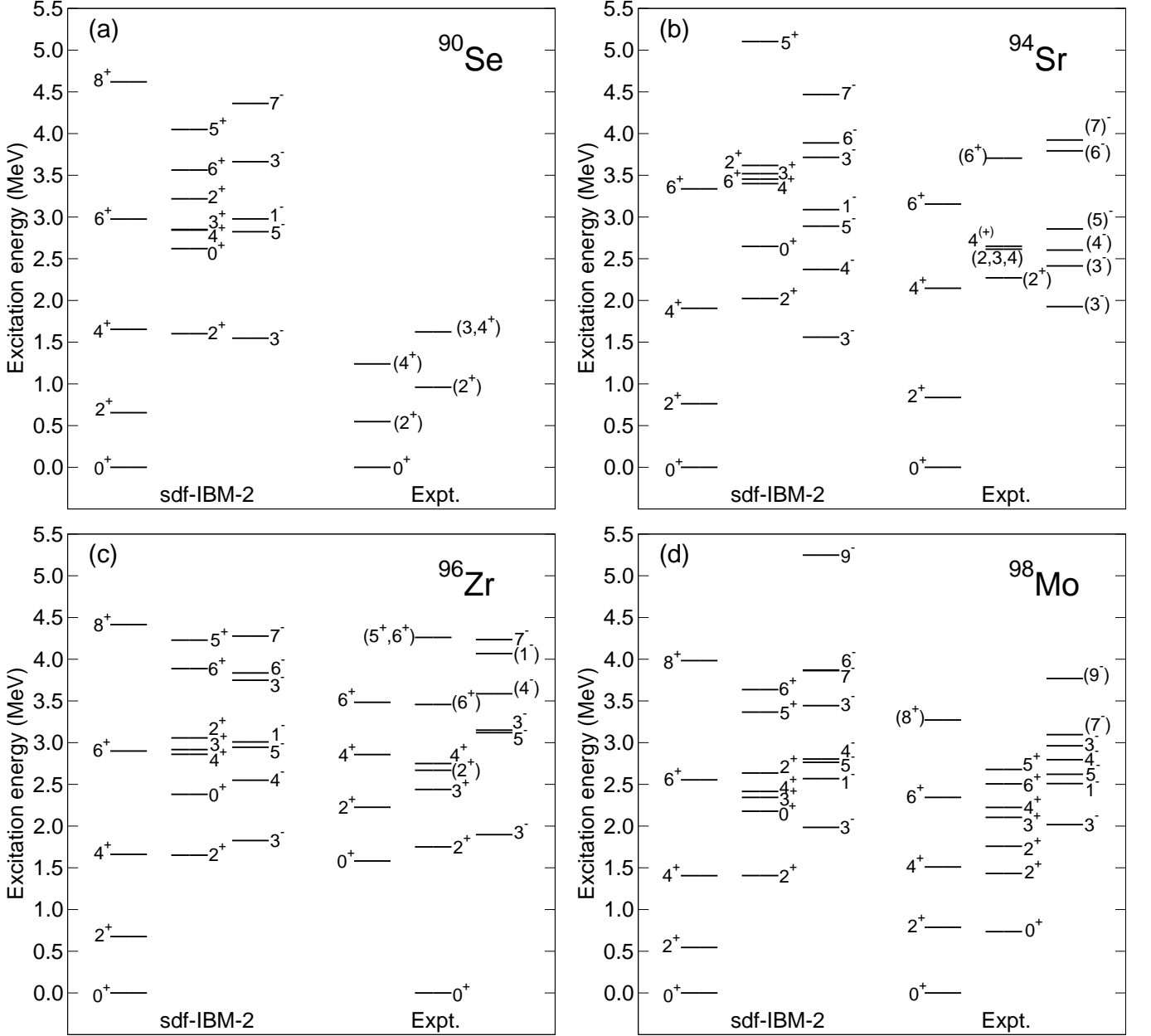


FIG. 13. Same as Fig. 10, but for the  $N = 56$  isotones (a)  $^{90}\text{Se}$ , (b)  $^{94}\text{Sr}$ , (c)  $^{96}\text{Zr}$ , and (d)  $^{98}\text{Mo}$ . The experimental data are taken from Refs. [84] ( $^{90}\text{Se}$ ), [83] ( $^{94}\text{Sr}$ ), [82] ( $^{96}\text{Zr}$ ), and [10, 93] ( $^{98}\text{Mo}$ ).

sonable description of the experimental data.

The electromagnetic transition properties of the low-lying states in  $^{96}\text{Zr}$  computed by the mapped *sdf*-IBM-2 Hamiltonian are shown in Table III, together with the experimental data [82, 91]. Some disagreements between the calculated and experimental  $E2$  transition properties for  $^{96}\text{Zr}$ , especially those related to the positive-parity states, are mainly due to the lack of the intruder configuration in the model. The predicted  $B(E3)$  values for the transitions from the odd-spin negative-parity states are noticeably large, particularly, for the  $\Delta I = 1$   $E3$

transitions.

The predicted low-energy spectrum for  $^{98}\text{Mo}$ , shown in Fig. 13(d), is basically similar to the one for  $^{96}\text{Zr}$ . Comparing with the experimental data [10, 82, 93], the predicted  $K = 0_1^+$  band suggests a slightly stronger quadrupole collectivity with the ratio  $R_{4/2} = 2.58$ . The calculated  $0_2^+$  excitation energy  $E_x(0_2^+) = 2178$  keV is much higher than the experimental counterpart  $E_x(0_2^+) = 735$  keV. Experimentally, the  $0_2^+$  state is also the first excited state of  $^{98}\text{Mo}$ . As already remarked, the  $0_2^+$  level could be lowered by the inclusion of the config-

TABLE II. Same as Table I, but for  $^{90}\text{Se}$  and  $^{94}\text{Sr}$ .

	$^{90}\text{Se}$	$^{94}\text{Sr}$
$B(E2; 2_1^+ \rightarrow 0_1^+)$	14	20
$B(E2; 2_2^+ \rightarrow 0_1^+)$	0.29	0.68
$B(E2; 2_2^+ \rightarrow 2_1^+)$	18	21
$B(E2; 4_1^+ \rightarrow 2_1^+)$	19	29
$B(E2; 4_2^+ \rightarrow 2_1^+)$	0.047	0.14
$B(E2; 4_2^+ \rightarrow 2_2^+)$	11	17
$B(E2; 4_2^+ \rightarrow 4_1^+)$	9.3	12
$B(E2; 3_1^+ \rightarrow 2_1^+)$	0.24	0.86
$B(E2; 3_1^+ \rightarrow 2_2^+)$	14	21
$B(E2; 3_2^- \rightarrow 3_1^-)$	0.015	0.54
$B(M1; 2_2^+ \rightarrow 2_1^+)$	0.001	0.00039
$B(M1; 3_1^+ \rightarrow 2_1^+)$	0.00015	0.00012
$B(M1; 3_1^+ \rightarrow 2_2^+)$	0.0032	0.00037
$B(M1; 4_2^+ \rightarrow 4_1^+)$	0.0025	0.0017
$B(M1; 3_2^- \rightarrow 3_1^-)$	0.014	0.017
$B(E1; 1_1^- \rightarrow 0_1^+)$	$1.0 \times 10^{-4}$	$7.6 \times 10^{-5}$
$B(E1; 3_2^- \rightarrow 2_1^+)$	$1.7 \times 10^{-5}$	$8.8 \times 10^{-5}$
$B(E1; 3_1^- \rightarrow 2_1^+)$	$2.0 \times 10^{-4}$	$1.4 \times 10^{-4}$
$B(E1; 3_1^- \rightarrow 2_2^+)$	$5.6 \times 10^{-4}$	$5.5 \times 10^{-4}$
$B(E1; 3_1^- \rightarrow 4_1^+)$	$4.5 \times 10^{-7}$	$2.2 \times 10^{-8}$
$B(E1; 5_1^- \rightarrow 4_1^+)$	$5.3 \times 10^{-4}$	$3.8 \times 10^{-4}$
$B(E1; 7_1^- \rightarrow 6_1^+)$	$1.1 \times 10^{-3}$	$6.9 \times 10^{-4}$
$B(E3; 3_1^- \rightarrow 0_1^+)$	17	20
$B(E3; 3_1^- \rightarrow 2_1^+)$	42	36
$B(E3; 3_1^- \rightarrow 4_1^+)$	12	6.6
$B(E3; 5_1^- \rightarrow 2_1^+)$	12	13
$B(E3; 5_1^- \rightarrow 4_1^+)$	33	31
$B(E3; 7_1^- \rightarrow 4_1^+)$	11	12
$B(E3; 7_1^- \rightarrow 6_1^+)$	30	19
$Q(2_1^+)$	0.087	0.24
$\mu(2_1^+)$	0.31	0.39

uration mixing between the normal and intruder states. A previous mapped IBM-2 configuration-mixing calculation, which is based on a Skyrme-type EDF, showed [93] that the coexistence of a nearly spherical prolate and  $\gamma$ -soft prolate SCMF minima is present in  $^{98}\text{Mo}$  and that the  $0_2^+$  state is characterized by the strong mixing between the nearly spherical normal configuration and the deformed intruder configuration arising from the proton  $2p - 2h$  excitation across the  $Z = 40$  sub-shell closure. On the other hand, the observed negative-parity states up to the  $4_1^-$  state are reasonably reproduced. Some relevant electromagnetic properties for  $^{98}\text{Mo}$  resulting from the mapped *sdf*-IBM-2 calculation are shown in Table IV in comparison to the available data [82, 93]. The agreement with the experimental data is fair. The calculation suggests strong  $\Delta I = 3$  *E3* transitions of the odd-spin negative-parity to the even-spin positive-parity yrast states.

TABLE III.  $B(E2)$ ,  $B(M1)$ ,  $B(E3)$ , and  $B(E1)$  transition rates (in W.u.), and the electric quadrupole  $Q(I)$  (in *eb*), and magnetic dipole  $\mu(I)$  (in  $\mu_N$ ) moments, predicted by the mapped *sdf*-IBM-2 for  $^{96}\text{Zr}$  in comparison to the available experimental data [82, 91].

	<i>sdf</i> -IBM-2	Experiment
$B(E2; 0_3^+ \rightarrow 2_2^+)$	11	$34 \pm 9$
$B(E2; 2_1^+ \rightarrow 0_1^+)$	21	$2.3 \pm 0.3$
$B(E2; 2_2^+ \rightarrow 2_1^+)$	26	$> 0.16$
$B(E2; 2_2^+ \rightarrow 0_2^+)$	4.5	$36 \pm 11$
$B(E2; 2_2^+ \rightarrow 0_1^+)$	0.31	$0.26 \pm 0.08$
$B(E2; 2_3^+ \rightarrow 2_1^+)$	0.079	$(5.0 \pm 0.7)E + 1$
$B(E2; 3_1^+ \rightarrow 2_1^+)$	0.43	$0.1_{-0.1}^{+0.3}$
$B(E2; 4_1^+ \rightarrow 2_2^+)$	0.0016	$56_{-44}^{+20}$
$B(E2; 4_1^+ \rightarrow 2_1^+)$	29	$16_{-5}^{+3}$
$B(E2; 4_2^+ \rightarrow 2_1^+)$	0.068	$16_{-13}^{+5}$
$B(E2; 4_3^+ \rightarrow 2_2^+)$	0.17	$< 1.6$
$B(E2; 3_2^- \rightarrow 3_1^-)$	1.7	$< 4.2$
$B(E2; 5_1^- \rightarrow 3_1^-)$	10	$14_{-14}^{+5}$
$B(M1; 2_2^+ \rightarrow 2_1^+)$	0.00082	$0.14 \pm 0.05$
$B(M1; 2_3^+ \rightarrow 2_1^+)$	0.022	$0.04 \pm 0.06$
$B(M1; 3_1^+ \rightarrow 2_1^+)$	$9.0 \times 10^{-5}$	$0.18_{-0.09}^{+0.05}$
$B(M1; 3_2^- \rightarrow 3_1^-)$	0.011	$< 0.0027$
$B(E1; 1_1^- \rightarrow 0_1^+)$	$1.1 \times 10^{-4}$	
$B(E1; 2_2^+ \rightarrow 3_1^-)$	$7.1 \times 10^{-4}$	$(2.8 \pm 0.9) \times 10^{-3}$
$B(E1; 2_3^+ \rightarrow 3_1^-)$	$1.4 \times 10^{-5}$	$(0.0007_{-0.0007}^{+0.0004})$
$B(E1; 4_1^+ \rightarrow 3_1^-)$	$5.1 \times 10^{-7}$	$(7.0_{-0.6}^{+0.3})E - 5$
$B(E1; 4_3^+ \rightarrow 3_1^-)$	$8.3 \times 10^{-7}$	$< 0.00010$
$B(E1; 3_1^- \rightarrow 2_1^+)$	$2.1 \times 10^{-4}$	$0.00123 \pm 0.00010$
$B(E1; 3_2^- \rightarrow 3_1^+)$	$1.8 \times 10^{-4}$	$< 0.00100$
$B(E1; 5_1^- \rightarrow 4_1^+)$	$5.3 \times 10^{-4}$	
$B(E1; 7_1^- \rightarrow 6_1^+)$	$1.0 \times 10^{-3}$	
$B(E3; 3_1^- \rightarrow 0_1^+)$	21	$57 \pm 4$
$B(E3; 3_1^- \rightarrow 0_2^+)$	0.069	
$B(E3; 3_1^- \rightarrow 2_1^+)$	38	
$B(E3; 5_1^- \rightarrow 2_1^+)$	17	
$B(E3; 5_1^- \rightarrow 4_1^+)$	32	
$B(E3; 7_1^- \rightarrow 4_1^+)$	15	
$B(E3; 7_1^- \rightarrow 6_1^+)$	28	
$Q(2_1^+)$	0.17	
$Q(3_1^-)$	-0.42	$+2.9 \pm 0.5$
$\mu(2_1^+)$	0.4	$+0.06 \pm 0.14$

#### IV. CONCLUDING REMARKS

Octupole correlations and the related spectroscopic properties of the neutron-rich  $A \approx 100$  nuclei near the empirical octupole magic numbers  $Z = 34$  and  $N = 56$  have been investigated based on the nuclear density functional theory and the mapped *sdf*-IBM-2 framework. The axially-symmetric quadrupole and octupole constrained SCMF calculations using the relativistic DD-PC1 EDF and the separable pairing force of finite range have been carried out to provide the potential energy surfaces for the considered even-even nuclei  $^{86-94}\text{Se}$ ,  $^{88-96}\text{Kr}$ ,  $^{90-98}\text{Sr}$ ,  $^{92-100}\text{Zr}$ , and  $^{94-102}\text{Mo}$  as functions of

TABLE IV. Same as Table III, but for  $^{98}\text{Mo}$ . The experimental data are taken from Refs. [10, 82, 93].

	<i>sdf</i> -IBM-2	Experiment
$B(E2; 2_1^+ \rightarrow 0_1^+)$	18	$20.1 \pm 0.4$
$B(E2; 2_1^+ \rightarrow 0_2^+)$	0.35	$9.7^{+1.0}_{-2.5}$
$B(E2; 2_2^+ \rightarrow 0_1^+)$	0.36	$1.02^{+0.15}_{-0.12}$
$B(E2; 2_2^+ \rightarrow 0_2^+)$	4.3	$2.3^{+0.5}_{-0.4}$
$B(E2; 2_2^+ \rightarrow 2_1^+)$	17	$48^{+9}_{-8}$
$B(E2; 2_3^+ \rightarrow 4_1^+)$	0.037	$14 \pm 4$
$B(E2; 2_3^+ \rightarrow 2_2^+)$	0.11	$< 22$
$B(E2; 2_3^+ \rightarrow 2_1^+)$	0.19	$3.0 \pm 0.7$
$B(E2; 2_3^+ \rightarrow 0_2^+)$	0.36	$7.5^{+0.6}_{-0.5}$
$B(E2; 2_3^+ \rightarrow 0_1^+)$	0.0033	$0.032^{+0.007}_{-0.006}$
$B(E2; 2_4^+ \rightarrow 2_1^+)$	0.00031	$> 0.49$
$B(E2; 4_1^+ \rightarrow 2_1^+)$	25	$42.3^{+0.9}_{-0.8}$
$B(E2; 4_1^+ \rightarrow 2_2^+)$	0.023	$15.2^{+3.3}_{-3.0}$
$B(E2; 6_1^+ \rightarrow 4_1^+)$	26	$10.1 \pm 0.4$
$B(E2; 3_2^- \rightarrow 3_1^-)$	0.5	
$B(M1; 2_2^+ \rightarrow 2_1^+)$	0.0021	$0.0073^{+0.0023}_{-0.0017}$
$B(M1; 2_3^+ \rightarrow 2_2^+)$	0.00013	$0.0157^{+0.0027}_{-0.0034}$
$B(M1; 2_3^+ \rightarrow 2_1^+)$	0.023	$0.0032^{+0.0008}_{-0.0007}$
$B(M1; 2_4^+ \rightarrow 2_1^+)$	0.0016	$> 0.019$
$B(M1; 2_5^+ \rightarrow 2_2^+)$	0.0019	$> 0.054$
$B(M1; 3_2^- \rightarrow 3_1^-)$	0.013	
$B(E1; 1_1^- \rightarrow 0_1^+)$	$2.5 \times 10^{-4}$	
$B(E1; 3_1^- \rightarrow 2_3^+)$	$1.9 \times 10^{-5}$	$(4.9^{+0.9}_{-0.7}) \times 10^{-5}$
$B(E1; 3_1^- \rightarrow 4_1^+)$	$4.0 \times 10^{-6}$	$(1.02^{+0.31}_{-0.24}) \times 10^{-6}$
$B(E1; 3_1^- \rightarrow 2_2^+)$	$1.8 \times 10^{-4}$	$< 5.7 \times 10^{-8}$
$B(E1; 3_1^- \rightarrow 2_1^+)$	$6.8 \times 10^{-4}$	$(1.76^{+0.28}_{-0.22}) \times 10^{-6}$
$B(E1; 3_2^- \rightarrow 2_1^+)$	$3.8 \times 10^{-5}$	
$B(E1; 3_2^- \rightarrow 2_2^+)$	$1.5 \times 10^{-4}$	
$B(E1; 5_1^- \rightarrow 4_1^+)$	$1.3 \times 10^{-3}$	
$B(E1; 7_1^- \rightarrow 6_1^+)$	$1.9 \times 10^{-3}$	
$B(E3; 3_1^- \rightarrow 0_2^+)$	0.038	$< 58$
$B(E3; 3_1^- \rightarrow 0_1^+)$	21	$30^{+7}_{-5}$
$B(E3; 3_1^- \rightarrow 2_1^+)$	25	
$B(E3; 3_1^- \rightarrow 2_2^+)$	5.2	
$B(E3; 3_2^- \rightarrow 2_1^+)$	0.17	
$B(E3; 3_2^- \rightarrow 2_2^+)$	1.8	
$B(E3; 5_1^- \rightarrow 2_1^+)$	26	
$B(E3; 5_1^- \rightarrow 4_1^+)$	19	
$B(E3; 7_1^- \rightarrow 4_1^+)$	25	
$B(E3; 7_1^- \rightarrow 6_1^+)$	18	
$Q(2_1^+)$	-0.25	$-0.26 \pm 0.09$
$\mu(2_1^+)$	0.31	$+0.97 \pm 0.06$

the  $\beta_2$  and  $\beta_3$  deformations. At the SCMF level, no non-zero  $\beta_3$  minimum was obtained on the  $\beta_2 - \beta_3$  energy surfaces, whereas the potential becomes soft in the  $\beta_3$  deformation around the neutron number  $N = 56$  for each of the considered isotopic chains. The excitation spectra for the low-lying states with both parities and the electromagnetic transition rates have been computed by the diagonalization of the *sdf*-IBM-2 Hamiltonian with the

strength parameters determined by mapping the SCMF energy surface onto the expectation value of the Hamiltonian in the boson condensate state.

Evolution of the predicted positive-parity yrast spectra has indicated a smooth onset of quadrupole collectivity in the Se, Kr, and Mo isotopes, and an abrupt nuclear structural change at  $N \approx 60$  in the Sr and Zr chains, as empirically suggested. The present theoretical analysis put much emphasis on the description of the negative-parity states. The predicted negative-parity odd-spin states show a parabolic dependence on  $N$  centered around  $N = 56$  at which the corresponding  $\beta_2 - \beta_3$  energy surface becomes softest along the  $\beta_3$  direction. The lowest negative-parity state  $3_1^-$  has been predicted to be typically at the excitation energy  $E_x \approx 1.5 - 2.5$  MeV, in a reasonable agreement with experiment. From the detailed comparisons between the calculated and experimental low-lying energy levels and transition properties for the  $N = 56$  isotones and some of the neutron-rich Kr nuclei that are of interest for recent measurements, the present calculation has produced finite  $E3$  transitions from the odd-spin negative-parity states to the ground-state band. These findings indicate the relevance of the octupole degrees of freedom in the description of the low-energy negative-parity states in the neutron-rich nuclei near the octupole magic numbers  $N = 56$  and  $Z = 34$  within the framework of the *sdf*-IBM-2.

For a more complete description of the low-energy states with both parities and their spectroscopy in this mass region, some extensions of the model will be required. In particular, the *sdf*-IBM-2 Hamiltonian has been here determined by the constrained SCMF calculations based only on the axially-symmetric shape degrees of freedom. On the other hand, the studied neutron-rich nuclei should have a more complex low-lying structure characterized, e.g., by the non-axial deformation and shape coexistence. Indeed, it has been revealed that the mapped *sdf*-IBM-2 employed in this paper is not able to describe the low-lying  $0_2^+$  state and the band built on it for the  $N > 56$  nuclei. The model would need to be extended in such a way that it simultaneously handles the octupole boson degrees of freedom, the triaxial deformation, and the intruder states and configuration mixing. Work along this direction is in progress and will be reported elsewhere.

## ACKNOWLEDGMENTS

This work is financed within the Tenure Track Pilot Programme of the Croatian Science Foundation and the École Polytechnique Fédérale de Lausanne, and the Project TTP-2018-07-3554 Exotic Nuclear Structure and Dynamics, with funds of the Croatian-Swiss Research Programme.

- [1] K. Heyde and J. L. Wood, *Rev. Mod. Phys.* **83**, 1467 (2011).
- [2] P. Cejnar, J. Jolie, and R. F. Casten, *Rev. Mod. Phys.* **82**, 2155 (2010).
- [3] P. A. Butler and W. Nazarewicz, *Rev. Mod. Phys.* **68**, 349 (1996).
- [4] P. A. Butler, *J. Phys. G: Nucl. Part. Phys.* **43**, 073002 (2016).
- [5] L. P. Gaffney, P. A. Butler, M. Scheck, A. B. Hayes, F. Wenander, M. Albers, B. Bastin, C. Bauer, A. Blazhev, S. Bönig, N. Bree, J. Cederkäll, T. Chupp, D. Cline, T. E. Cocolios, T. Davinson, H. D. Witte, J. Diriken, T. Grahn, A. Herzan, M. Huysse, D. G. Jenkins, D. T. Joss, N. Kesteloot, J. Konki, M. Kowalczyk, T. Kröll, E. Kwan, R. Lutter, K. Moschner, P. Napiorkowski, J. Pakarinen, M. Pfeiffer, D. Radeck, P. Reiter, K. Reynders, S. V. Rigby, L. M. Robledo, M. Rudigier, S. Sambi, M. Seidlitz, B. Siebeck, T. Stora, P. Thoele, P. V. Duppen, M. J. Vermeulen, M. von Schmid, D. Voulot, N. Warr, K. Wimmer, K. Wrzosek-Lipska, C. Y. Wu, and M. Zielinska, *Nature (London)* **497**, 199 (2013).
- [6] M. M. R. Chishti, D. O'Donnell, G. Battaglia, M. Bowry, D. A. Jaroszynski, B. S. N. Singh, M. Scheck, P. Spagnoletti, and J. F. Smith, *Nat. Phys.* **16**, 853 (2020).
- [7] B. Bucher, S. Zhu, C. Y. Wu, R. V. F. Janssens, D. Cline, A. B. Hayes, M. Albers, A. D. Ayangeakaa, P. A. Butler, C. M. Campbell, M. P. Carpenter, C. J. Chiara, J. A. Clark, H. L. Crawford, M. Cromaz, H. M. David, C. Dickerson, E. T. Gregor, J. Harker, C. R. Hoffman, B. P. Kay, F. G. Kondev, A. Korichi, T. Lauritsen, A. O. Macchiavelli, R. C. Pardo, A. Richard, M. A. Riley, G. Savard, M. Scheck, D. Seweryniak, M. K. Smith, R. Vondrasek, and A. Wiens, *Phys. Rev. Lett.* **116**, 112503 (2016).
- [8] B. Bucher, S. Zhu, C. Y. Wu, R. V. F. Janssens, R. N. Bernard, L. M. Robledo, T. R. Rodríguez, D. Cline, A. B. Hayes, A. D. Ayangeakaa, M. Q. Buckner, C. M. Campbell, M. P. Carpenter, J. A. Clark, H. L. Crawford, H. M. David, C. Dickerson, J. Harker, C. R. Hoffman, B. P. Kay, F. G. Kondev, T. Lauritsen, A. O. Macchiavelli, R. C. Pardo, G. Savard, D. Seweryniak, and R. Vondrasek, *Phys. Rev. Lett.* **118**, 152504 (2017).
- [9] T. Rzaca-Urban, W. Urban, A. Kaczor, J. L. Durell, M. J. Leddy, M. A. Jones, W. R. Phillips, A. G. Smith, B. J. Varley, I. Ahmad, L. R. Morss, M. Bentaleb, E. Lubkiewicz, and N. Schulz, *Eur. Phys. J. A* **9**, 165 (2000).
- [10] S. Lalkovski, S. Ilieva, A. Minkova, N. Minkov, T. Kutsarova, A. Lopez-Martens, A. Korichi, H. Hübel, A. Görgen, A. Jansen, G. Schönwasser, B. Herskind, M. Bergström, and Z. Podolyák, *Phys. Rev. C* **75**, 014314 (2007).
- [11] M. Scheck, P. A. Butler, C. Fransen, V. Werner, and S. W. Yates, *Phys. Rev. C* **81**, 064305 (2010).
- [12] K. LI, J. H. HAMILTON, A. V. RAMAYYA, S. H. LIU, X. Q. ZHANG, N. T. BREWER, J. K. HWANG, C. GOODIN, S. J. ZHU, Y. X. LUO, J. O. RASMUSSEN, I. Y. LEE, S. C. WU, R. DONANGELO, A. V. DANIEL, G. M. TER-AKOPIAN, Y. T. OGANESIAN, A. UNZHAKOVA, J. D. COLE, W. C. MA, and M. A. STOYER, *Int. J. Mod. Phys. E* **20**, 1825 (2011), <https://doi.org/10.1142/S0218301311019635>.
- [13] E. T. Gregor, M. Scheck, R. Chapman, L. P. Gaffney, J. Keatings, K. R. Mashtakov, D. O'Donnell, J. F. Smith, P. Spagnoletti, M. Thürauf, V. Werner, and C. Wiseman, *Eur. Phys. J. A* **53**, 50 (2017).
- [14] J. Dudouet, A. Lemasson, G. Duchêne, M. Rejmund, E. Clément, C. Michelagnoli, F. Didierjean, A. Korichi, G. Maquart, O. Stezowski, C. Lizarazo, R. M. Pérez-Vidal, C. Andreoiu, G. de Angelis, A. Astier, C. Delafosse, I. Deloncle, Z. Dombardi, G. de France, A. Gadea, A. Gottardo, B. Jacquot, P. Jones, T. Konstantinopoulos, I. Kuti, F. Le Blanc, S. M. Lenzi, G. Li, R. Lozeva, B. Million, D. R. Napoli, A. Navin, C. M. Petrache, N. Pietralla, D. Ralet, M. Ramdhane, N. Redon, C. Schmitt, D. Sohler, D. Verney, D. Barrientos, B. Birkenbach, I. Burrows, L. Charles, J. Collado, D. M. Cullen, P. Désesquelles, C. Domingo Pardo, V. González, L. Harkness-Brennan, H. Hess, D. S. Judson, M. Karolak, W. Korten, M. Labiche, J. Ljungvall, R. Menegazzo, D. Mengoni, A. Pullia, F. Recchia, P. Reiter, M. D. Salsac, E. Sanchis, C. Theisen, J. J. Valiente-Dobón, and M. Zielinska, *Phys. Rev. Lett.* **118**, 162501 (2017).
- [15] E. T. Gregor, N. N. Arsenyev, M. Scheck, T. M. Shneidman, M. Thürauf, C. Bernards, A. Blanc, R. Chapman, F. Drouet, A. A. Dzhioev, G. de France, M. Jentschel, J. Jolie, J. M. Keatings, T. Kröll, U. Köster, R. Leguillon, K. R. Mashtakov, P. Mutti, D. O'Donnell, C. M. Petrache, G. S. Simpson, J. Sinclair, J. F. Smith, T. Soldner, P. Spagnoletti, A. V. Sushkov, W. Urban, A. Vancraeynest, J. R. Vanhoy, V. Werner, K. O. Zell, and M. Zielinska, *J. Phys. G: Nucl. Part. Phys.* **46**, 075101 (2019).
- [16] R.-B. Gerst, A. Blazhev, K. Moschner, P. Doornenbal, A. Obertelli, K. Nomura, J.-P. Ebran, S. Hilaire, J. Libert, G. Authelet, H. Baba, D. Calvet, F. Château, S. Chen, A. Corsi, A. Delbart, J.-M. Gheller, A. Giganon, A. Gillibert, V. Lapoux, T. Motobayashi, M. Niikura, N. Paul, J.-Y. Roussé, H. Sakurai, C. Santamaria, D. Steppenbeck, R. Taniuchi, T. Uesaka, T. Ando, T. Arici, F. Browne, A. M. Bruce, R. Caroll, L. X. Chung, M. L. Cortés, M. Dewald, B. Ding, F. Flavigny, S. Franchoo, M. Górska, A. Gottardo, J. Jolie, A. Jungclauss, J. Lee, M. Lettmann, B. D. Linh, J. Liu, Z. Liu, C. Lizarazo, S. Momiyama, S. Nagamine, N. Nakatsuka, C. R. Nita, C. Nobs, L. Olivier, R. Orlandi, Z. Patel, Z. Podolyák, M. Rudigier, T. Saito, C. Shand, P.-A. Söderström, I. Stefan, V. Vaquero, V. Werner, K. Wimmer, and Z. Xu, *Phys. Rev. C* **105**, 024302 (2022).
- [17] W. Nazarewicz, P. Olanders, I. Ragnarsson, J. Dudek, G. A. Leander, P. Möller, and E. Ruchowska, *Nucl. Phys. A* **429**, 269 (1984).
- [18] G. Leander, W. Nazarewicz, P. Olanders, I. Ragnarsson, and J. Dudek, *Phys. Lett. B* **152**, 284 (1985).
- [19] P. Möller, R. Bengtsson, B. Carlsson, P. Olivius, T. Ichikawa, H. Sagawa, and A. Iwamoto, *At. Dat. Nucl. Dat. Tab.* **94**, 758 (2008).
- [20] P. Bonche, P.-H. Heenen, H. Flocard, and D. Vautherin, *Phys. Lett. B* **175**, 387 (1986).
- [21] P.-H. Heenen, J. Skalski, P. Bonche, and H. Flocard, *Phys. Rev. C* **50**, 802 (1994).

- [22] L. Robledo, J. Egido, J. Berger, and M. Girod, *Phys. Lett. B* **187**, 223 (1987).
- [23] J. Egido and L. Robledo, *Nucl. Phys. A* **545**, 589 (1992).
- [24] L. M. Robledo, M. Baldo, P. Schuck, and X. Viñas, *Phys. Rev. C* **81**, 034315 (2010).
- [25] L. M. Robledo and G. F. Bertsch, *Phys. Rev. C* **84**, 054302 (2011).
- [26] Z. P. Li, B. Y. Song, J. M. Yao, D. Vretenar, and J. Meng, *Phys. Lett. B* **726**, 866 (2013).
- [27] L. M. Robledo and P. A. Butler, *Phys. Rev. C* **88**, 051302 (2013).
- [28] J. M. Yao, E. F. Zhou, and Z. P. Li, *Phys. Rev. C* **92**, 041304 (2015).
- [29] R. N. Bernard, L. M. Robledo, and T. R. Rodríguez-Guzmán, *Phys. Rev. C* **93**, 061302 (2016).
- [30] S. Y. Xia, H. Tao, Y. Lu, Z. P. Li, T. Nikšić, and D. Vretenar, *Phys. Rev. C* **96**, 054303 (2017).
- [31] S. E. Agbemava and A. V. Afanasjev, *Phys. Rev. C* **96**, 024301 (2017).
- [32] S. Ebata and T. Nakatsukasa, *Phys. Scr.* **92**, 064005 (2017).
- [33] P. Marević, J.-P. Ebran, E. Khan, T. Nikšić, and D. Vretenar, *Phys. Rev. C* **97**, 024334 (2018).
- [34] L. M. Robledo, T. R. Rodríguez, and R. R. Rodríguez-Guzmán, *J. Phys. G: Nucl. Part. Phys.* **46**, 013001 (2019).
- [35] Y. Cao, S. E. Agbemava, A. V. Afanasjev, W. Nazarewicz, and E. Olsen, *Phys. Rev. C* **102**, 024311 (2020).
- [36] R. Rodríguez-Guzmán, Y. M. Humadi, and L. M. Robledo, *J. Phys. G: Nucl. Part. Phys.* **48**, 015103 (2020).
- [37] K. Nomura, L. Lotina, T. Nikšić, and D. Vretenar, *Phys. Rev. C* **103**, 054301 (2021).
- [38] J. Engel and F. Iachello, *Phys. Rev. Lett.* **54**, 1126 (1985).
- [39] J. Engel and F. Iachello, *Nucl. Phys. A* **472**, 61 (1987).
- [40] T. Otsuka, *Phys. Lett. B* **182**, 256 (1986).
- [41] T. Otsuka and M. Sugita, *Phys. Lett. B* **209**, 140 (1988).
- [42] M. Sugita, T. Otsuka, and P. von Brentano, *Phys. Lett. B* **389**, 642 (1996).
- [43] D. Kusnezov and F. Iachello, *Physics Letters B* **209**, 420 (1988).
- [44] N. Yoshinaga, T. Mizusaki, and T. Otsuka, *Nucl. Phys. A* **559**, 193 (1993).
- [45] N. V. Zamfir and D. Kusnezov, *Phys. Rev. C* **63**, 054306 (2001).
- [46] N. A. Smirnova, N. Pietralla, T. Mizusaki, and P. Van Isacker, *Nuclear Physics A* **678**, 235 (2000).
- [47] N. Pietralla, C. Fransen, A. Gade, N. A. Smirnova, P. von Brentano, V. Werner, and S. W. Yates, *Phys. Rev. C* **68**, 031305 (2003).
- [48] K. Nomura, D. Vretenar, and B.-N. Lu, *Phys. Rev. C* **88**, 021303 (2013).
- [49] K. Nomura, D. Vretenar, T. Nikšić, and B.-N. Lu, *Phys. Rev. C* **89**, 024312 (2014).
- [50] K. Nomura, R. Rodríguez-Guzmán, and L. M. Robledo, *Phys. Rev. C* **92**, 014312 (2015).
- [51] K. Nomura, R. Rodríguez-Guzmán, Y. M. Humadi, L. M. Robledo, and J. E. García-Ramos, *Phys. Rev. C* **102**, 064326 (2020).
- [52] K. Nomura, R. Rodríguez-Guzmán, L. Robledo, and J. García-Ramos, *Phys. Rev. C* **103**, 044311 (2021).
- [53] K. Nomura, R. Rodríguez-Guzmán, L. M. Robledo, J. E. García-Ramos, and N. C. Hernández, *Phys. Rev. C* **104**, 044324 (2021).
- [54] K. Nomura, R. Rodríguez-Guzmán, and L. M. Robledo, *Phys. Rev. C* **104**, 054320 (2021).
- [55] A. Hennig, M. Spieker, V. Werner, T. Ahn, V. Anagnostatou, N. Cooper, V. Derya, M. Elvers, J. Endres, P. Goddard, A. Heinz, R. O. Hughes, G. Ilie, M. N. Mineva, P. Petkov, S. G. Pickstone, N. Pietralla, D. Radeck, T. J. Ross, D. Savran, and A. Zilges, *Phys. Rev. C* **90**, 051302 (2014).
- [56] O. Vallejos and J. Barea, *Phys. Rev. C* **104**, 014308 (2021).
- [57] D. Bonatsos, D. Lenis, N. Minkov, D. Petrellis, and P. Yotov, *Phys. Rev. C* **71**, 064309 (2005).
- [58] D. Lenis and D. Bonatsos, *Phys. Lett. B* **633**, 474 (2006).
- [59] P. G. Bizzeti and A. M. Bizzeti-Sona, *Phys. Rev. C* **88**, 011305 (2013).
- [60] D. Bonatsos, A. Martinou, N. Minkov, S. Karampagia, and D. Petrellis, *Phys. Rev. C* **91**, 054315 (2015).
- [61] T. M. Shneidman, G. G. Adamian, N. V. Antonenko, R. V. Jolos, and W. Scheid, *Phys. Lett. B* **526**, 322 (2002).
- [62] T. M. Shneidman, G. G. Adamian, N. V. Antonenko, R. V. Jolos, and W. Scheid, *Phys. Rev. C* **67**, 014313 (2003).
- [63] R. V. Jolos, P. von Brentano, and J. Jolie, *Phys. Rev. C* **86**, 024319 (2012).
- [64] B. A. Brown, *Phys. Rev. Lett.* **85**, 5300 (2000).
- [65] K. Kaneko, M. Hasegawa, and T. Mizusaki, *Phys. Rev. C* **66**, 051306 (2002).
- [66] N. Yoshinaga, K. Yanase, K. Higashiyama, and E. Teruya, *Phys. Rev. C* **98**, 044321 (2018).
- [67] P. Van Isacker, *Eur. Phys. J. Special Topics* **229**, 2443 (2010).
- [68] M. Bender, P.-H. Heenen, and P.-G. Reinhard, *Rev. Mod. Phys.* **75**, 121 (2003).
- [69] D. Vretenar, A. V. Afanasjev, G. A. Lalazissis, and P. Ring, *Phys. Rep.* **409**, 101 (2005).
- [70] T. Nikšić, D. Vretenar, and P. Ring, *Prog. Part. Nucl. Phys.* **66**, 519 (2011).
- [71] P. Ring and P. Schuck, *The Nuclear Many-Body Problem* (Springer-Verlag, Berlin, 1980).
- [72] T. Nikšić, D. Vretenar, and P. Ring, *Phys. Rev. C* **78**, 034318 (2008).
- [73] T. Nikšić, N. Paar, D. Vretenar, and P. Ring, *Comput. Phys. Commun.* **185**, 1808 (2014).
- [74] Y. Tian, Z. Y. Ma, and P. Ring, *Phys. Lett. B* **676**, 44 (2009).
- [75] T. Otsuka, A. Arima, F. Iachello, and I. Talmi, *Phys. Lett. B* **76**, 139 (1978).
- [76] T. Otsuka, A. Arima, and F. Iachello, *Nucl. Phys. A* **309**, 1 (1978).
- [77] J. N. Ginocchio and M. W. Kirson, *Nucl. Phys. A* **350**, 31 (1980).
- [78] K. Nomura, N. Shimizu, and T. Otsuka, *Phys. Rev. Lett.* **101**, 142501 (2008).
- [79] K. Nomura, N. Shimizu, and T. Otsuka, *Phys. Rev. C* **81**, 044307 (2010).
- [80] S. Heinze, computer program ARBMODEL, University of Cologne (2008).
- [81] G. A. Lalazissis, T. Nikšić, D. Vretenar, and P. Ring, *Phys. Rev. C* **71**, 024312 (2005).
- [82] Brookhaven National Nuclear Data Center, <http://www.nndc.bnl.gov>.

- [83] T. Rzaca-Urban, K. Sieja, W. Urban, F. Nowacki, J. L. Durell, A. G. Smith, and I. Ahmad, *Phys. Rev. C* **79**, 024319 (2009).
- [84] S. Chen, P. Doornenbal, A. Obertelli, T. R. Rodríguez, G. Authelet, H. Baba, D. Calvet, F. Château, A. Corsi, A. Delbart, J.-M. Gheller, A. Giganon, A. Gillibert, V. Lapoux, T. Motobayashi, M. Niikura, N. Paul, J.-Y. Roussé, H. Sakurai, C. Santamaria, D. Steppenbeck, R. Taniuchi, T. Uesaka, T. Ando, T. Arici, A. Blazhev, F. Browne, A. M. Bruce, R. Caroll, L. X. Chung, M. L. Cortés, M. Dewald, B. Ding, F. Flavigny, S. Franchoo, M. Górska, A. Gottardo, A. Jungclaus, J. Lee, M. Lettmann, B. D. Linh, J. Liu, Z. Liu, C. Lizarazo, S. Momiyama, K. Moschner, S. Nagamine, N. Nakatsuka, C. R. Nita, C. Nobs, L. Olivier, R. Orlandi, Z. Patel, Z. Podolyak, M. Rudigier, T. Saito, C. Shand, P.-A. Söderström, I. Stefan, V. Vaquero, V. Werner, K. Wimmer, and Z. Xu, *Phys. Rev. C* **95**, 041302 (2017).
- [85] C. Lizarazo, P.-A. Söderström, V. Werner, N. Pietralla, P. M. Walker, G. X. Dong, F. R. Xu, T. R. Rodríguez, F. Browne, P. Doornenbal, S. Nishimura, C. R. Niță, A. Obertelli, T. Ando, T. Arici, G. Authelet, H. Baba, A. Blazhev, A. M. Bruce, D. Calvet, R. J. Caroll, F. Château, S. Chen, L. X. Chung, A. Corsi, M. L. Cortés, A. Delbart, M. Dewald, B. Ding, F. Flavigny, S. Franchoo, J. Gerl, J.-M. Gheller, A. Giganon, A. Gillibert, M. Górska, A. Gottardo, I. Kojouharov, N. Kurz, V. Lapoux, J. Lee, M. Lettmann, B. D. Linh, J. J. Liu, Z. Liu, S. Momiyama, K. Moschner, T. Motobayashi, S. Nagamine, N. Nakatsuka, M. Niikura, C. Nobs, L. Olivier, Z. Patel, N. Paul, Z. Podolyák, J.-Y. Roussé, M. Rudigier, T. Y. Saito, H. Sakurai, C. Santamaria, H. Schaffner, C. Shand, I. Stefan, D. Steppenbeck, R. Taniuchi, T. Uesaka, V. Vaquero, K. Wimmer, and Z. Xu, *Phys. Rev. Lett.* **124**, 222501 (2020).
- [86] R.-B. Gerst, A. Blazhev, N. Warr, J. N. Wilson, M. Lebois, N. Jovančević, D. Thisse, R. Canavan, M. Rudigier, D. Étasse, E. Adamska, P. Adsley, A. Algora, M. Babo, K. Belvedere, J. Benito, G. Benzoni, A. Boso, S. Bottoni, M. Bunce, R. Chakma, N. Cieplicka-Oryńczak, S. Courtin, M. L. Cortés, P. Davies, C. Delafosse, M. Fallot, B. Fornal, L. M. Fraile, D. Gjestvang, A. Gottardo, V. Guadilla, G. Häfner, K. Hauschild, M. Heine, C. Henrich, I. Homm, F. Ibrahim, L. W. Iskra, P. Ivanov, S. Jazrawi, A. Korgul, P. Koseoglou, T. Kröll, T. Kurtukian-Nieto, L. Le Meur, S. Leoni, J. Ljungvall, A. Lopez-Martens, R. Lozeva, I. Matea, K. Miernik, J. Nemer, S. Oberstedt, W. Paulsen, M. Piersa, Y. Popovitch, C. Porzio, L. Qi, D. Ralet, P. H. Regan, D. Reygadas-Tello, K. Rezyunkina, V. Sánchez-Tembleque, C. Schmitt, P.-A. Söderström, C. Sürder, G. Tocabens, V. Vedia, D. Verney, B. Wasilewska, J. Wiederhold, M. Yavachova, F. Zeiser, and S. Ziliani, *Phys. Rev. C* **102**, 064323 (2020).
- [87] M. Albers, N. Warr, K. Nomura, A. Blazhev, J. Jolie, D. Mücher, B. Bastin, C. Bauer, C. Bernards, L. Bettermann, V. Bildstein, J. Butterworth, M. Cappellazzo, J. Cederkäll, D. Cline, I. Darby, S. Das Gupta, J. M. Daugas, T. Davinson, H. De Witte, J. Diriken, D. Filipescu, E. Fiori, C. Fransen, L. P. Gaffney, G. Georgiev, R. Gernhäuser, M. Hackstein, S. Heinze, H. Hess, M. Huyse, D. Jenkins, J. Konki, M. Kowalczyk, T. Kröll, R. Krücken, J. Litzinger, R. Lutter, N. Marginean, C. Mihai, K. Moschner, P. Napiorkowski, B. S. Nara Singh, K. Nowak, T. Otsuka, J. Pakarinen, M. Pfeiffer, D. Radeck, P. Reiter, S. Rigby, L. M. Robledo, R. Rodríguez-Guzmán, M. Rudigier, P. Sarriguren, M. Scheck, M. Seidlitz, B. Siebeck, G. Simpson, P. Thöle, T. Thomas, J. Van de Walle, P. Van Duppen, M. Vermeulen, D. Voulot, R. Wadsworth, F. Wenander, K. Wimmer, K. O. Zell, and M. Zielinska, *Phys. Rev. Lett.* **108**, 062701 (2012).
- [88] T. Kibédi and R. H. Spear, *At. Data and Nucl. Data Tables* **80**, 35 (2002).
- [89] E. Elhami, J. N. Orce, M. Scheck, S. Mukhopadhyay, S. N. Choudry, M. T. McEllistrem, S. W. Yates, C. Angell, M. Boswell, B. Fallin, C. R. Howell, A. Hutcheon, H. J. Karwowski, J. H. Kelley, Y. Parpottas, A. P. Tonchev, and W. Tornow, *Phys. Rev. C* **78**, 064303 (2008).
- [90] M. Albers, K. Nomura, N. Warr, A. Blazhev, J. Jolie, D. Mücher, B. Bastin, C. Bauer, C. Bernards, L. Bettermann, V. Bildstein, J. Butterworth, M. Cappellazzo, J. Cederkäll, D. Cline, I. Darby, S. Das Gupta, J. Daugas, T. Davinson, H. De Witte, J. Diriken, D. Filipescu, E. Fiori, C. Fransen, L. Gaffney, G. Georgiev, R. Gernhäuser, M. Hackstein, S. Heinze, H. Hess, M. Huyse, D. Jenkins, J. Konki, M. Kowalczyk, T. Kröll, R. Krücken, J. Litzinger, R. Lutter, N. Marginean, C. Mihai, K. Moschner, P. Napiorkowski, B. Nara Singh, K. Nowak, J. Pakarinen, M. Pfeiffer, D. Radeck, P. Reiter, S. Rigby, L. Robledo, R. Rodríguez-Guzmán, M. Rudigier, M. Scheck, M. Seidlitz, B. Siebeck, G. Simpson, P. Thöle, T. Thomas, J. Van de Walle, P. Van Duppen, M. Vermeulen, D. Voulot, R. Wadsworth, F. Wenander, K. Wimmer, K. Zell, and M. Zielinska, *Nucl. Phys. A* **899**, 1 (2013).
- [91] C. Kremer, S. Aslanidou, S. Bassauer, M. Hilcker, A. Krugmann, P. von Neumann-Cosel, T. Otsuka, N. Pietralla, V. Y. Ponomarev, N. Shimizu, M. Singer, G. Steinhilber, T. Togashi, Y. Tsunoda, V. Werner, and M. Zweidinger, *Phys. Rev. Lett.* **117**, 172503 (2016).
- [92] F. Iachello and A. Arima, *The interacting boson model* (Cambridge University Press, Cambridge, 1987).
- [93] T. Thomas, K. Nomura, V. Werner, T. Ahn, N. Cooper, H. Duckwitz, M. Hinton, G. Ilie, J. Jolie, P. Petkov, and D. Radeck, *Phys. Rev. C* **88**, 044305 (2013).
- [94] T. Togashi, Y. Tsunoda, T. Otsuka, and N. Shimizu, *Phys. Rev. Lett.* **117**, 172502 (2016).